Project Report
TIP-189

The NIFTy Sensor for Methane Leak Detection Study: FY22 Climate Initiative Technical Investment Program

J.B. Ashcom
C.A. Primmerman
G. Ni

16 March 2023

Lincoln Laboratory
MASSACHUSETTS INSTITUTE OF TECHNOLOGY
LEXINGTON, MASSACHUSETTS

This material is based upon work supported by the Department of the Air Force under Air Force Contract No. FA8702-15-D-0001.

This report is the result of studies performed at Lincoln Laboratory, a federally funded research and development center operated by Massachusetts Institute of Technology. This material is based upon work supported by the Department of the Air Force under Air Force Contract No. FA8702-15-D-0001. Any opinions, findings, conclusions or recommendations expressed in this material are those of the author(s) and do not necessarily reflect the views of the Department of the Air Force.

Massachusetts Institute of Technology
Lincoln Laboratory

The NIFTy Sensor for Methane Leak Detection Study: FY22 Climate Initiative Technical Investment Program

J.B. Ashcom
Group 91

C.A. Primmerman
Division 9

G. Ni
Formerly of Group 74

Project Report TIP-189

16 March 2023

This material is based upon work supported by the Department of the Air Force under Air Force Contract No. FA8702-15-D-0001.

Lexington Massachusetts

This page intentionally left blank.

TABLE OF CONTENTS

This page intentionally left blank.

LIST OF ILLUSTRATIONS

LIST OF ILLUSTRATIONS
(Continued)

LIST OF TABLES

This page intentionally left blank.

1. ATMOSPHERIC METHANE SCIENCE AND REQUIREMENTS

1.1 STUDY STRUCTURE

Methane is a powerful greenhouse gas, roughly 80 times more potent than carbon dioxide in heat-trapping capacity [1, 2, 3]. It is receiving significant attention because reducing methane emissions offers a near-term way to reduce the overall atmospheric greenhouse gas load: a significant fraction of methane input into the atmosphere is anthropogenic, and the lifetime of methane in the atmosphere is relatively short, about nine years. Therefore, reducing the release of methane can be a high-impact path that countries can pursue to meet their commitments to greenhouse-gas reduction. This fact is leading to new regulations on the oil and gas industry as to what levels of natural gas leaks must be searched for and mitigated. In addition, there is renewed attention to increasing our understanding of the worldwide abundance of methane in the atmosphere and, consequently, to better measuring the various natural and manmade sources and sinks.

The Climate Initiative-funded FY2022 Methane Study was set up to explore how unique Lincoln Laboratory technology could support methane detection, both for global measurements to support better modeling of climate change, and for wide-area leak detection to support mitigation efforts. The approach began with a review of the methane-detection requirements and current technical approaches, so that gaps and limitations with current systems could be identified. The study then focused on several technical areas where the Laboratory could make the most immediate impact. On the global-measurement side, the study focused on traditional imaging spectrometers, but with improved spectral resolution and SWaP, and with the potential for complementary microwave-sounding measurements for improved accuracy. For leak detection, the study looked at the potential for methane detection of a novel Laboratory sensor developed to detect other gases—the NIFTy (Narrowband Imaging Filter Technology) optical system for high-sensitivity, high-area-coverage passive gas detection.

This report is divided into two parts. Section 1 summarizes the review of methane-sensing requirements and current state of the art. Section 2 presents the detailed analysis of the suitability of the NIFTy sensor for methane detection and the resulting notional system concept and performance predictions. The report on imaging spectrometers optimized for methane detection is presented in a separate document [4].

1.2 CURRENT UNDERSTANDING OF ATMOSPHERIC METHANE

As stated above, methane is a powerful greenhouse gas, and it is receiving a lot of attention. In 2021, there was a Global Methane Pledge to reduce methane emissions by at least 30% from 2020 levels by 2030. Worldwide, 151 countries have signed this pledge, including the USA and all EU countries (but not China, India, or Russia). Despite the pledge and other emphases on methane, there are major gaps in our understanding of atmospheric methane. Figure 1 shows some of the knowns and unknowns regarding atmospheric methane [5].

It is accepted that the global concentration of methane is ~1,900 ppb—about 2-3 times the pre-industrial concentration. It is known that the sources of methane emissions are varied and widely dispersed. Major sources include coal mining, oil and gas production and distribution, waste-disposal landfills, agriculture (particularly rice cultivation), and enteric fermentation in cows. Estimates of total methane

emissions vary widely—from 550 to 880 Tg/year. It is well known that methane is removed from the atmosphere by reaction with OH, but estimates of the total amount removed per year also vary widely—from 500 to 800 TG/year.

The lower right-hand plot in Figure 1 shows the global methane concentration over the last 20 years. It is observed that from about 2000 to 2006 the global concentration was about constant but that recently the concentration has grown at an increasing rate. No one has a good explanation for either behavior. It seems clear that better sensing of atmospheric methane is needed [6].

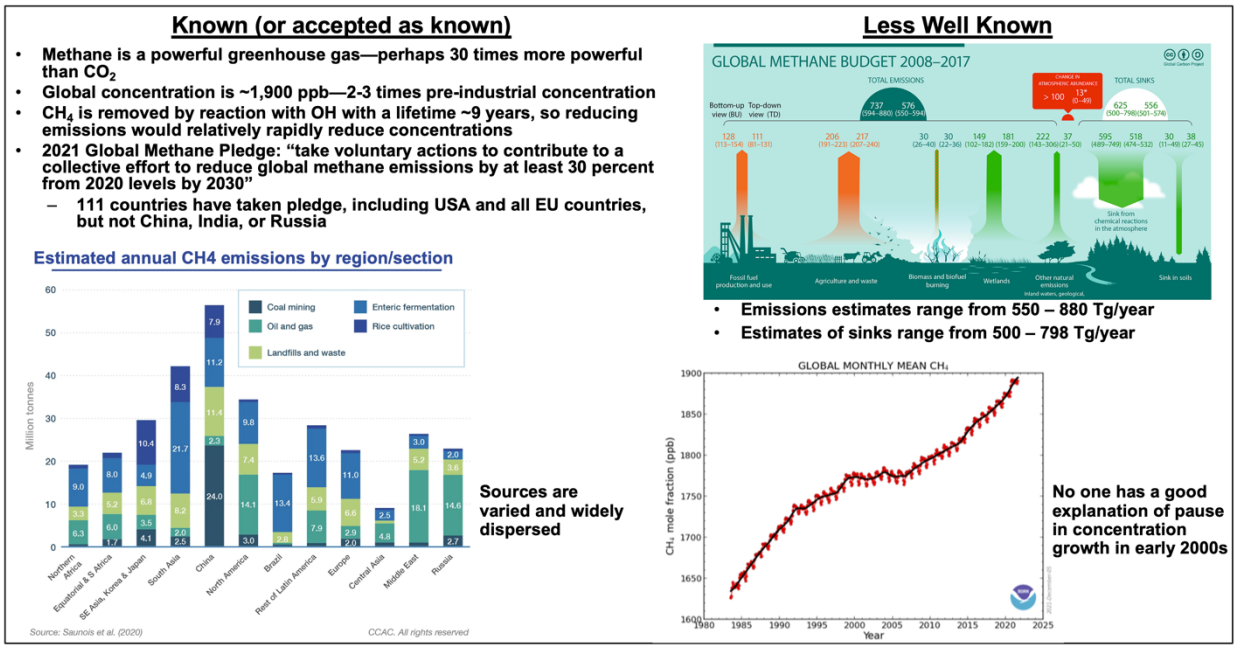

Figure 1. Atmospheric methane knowns and unknowns.

Table 1 lists some important considerations for improved sensing of atmospheric methane. It has been observed, particularly with regard to the oil and gas industry, that the emissions can be dominated by infrequent, very large releases [7, 8, 9]. This fact implies that measurements must be made at a high temporal cadence. Unfortunately, satellite revisits and aircraft scheduling may result in weeks to months between revisits—clearly much too long.

The varied, worldwide sources of methane emissions imply that one needs to sense all over the world and at all times of the day in order to gather meaningful data. Many of the current sensors, however, are absorption spectrometers that sense reflected sunlight at 1.65 μm or 2.3 μm. These have no capability at night and very little capability over water and at high latitudes.

To effectively mitigate large leaks (which may dominate emissions in the oil and gas industry) the leaks must be fixed rapidly. The requirement for rapid fixing suggests that near-real-time processing may be required. In contrast, retrieving methane concentrations from spectrometer measurements currently requires complex calculations that may take days to months.

Finally, if there are multiple sources of methane present (e.g., both gas production and landfills), it may be desirable to sense different isotopes of methane. For instance, the ratio of $^{12}CH_4$ to $^{13}CH_4$ can, in

principle, be used to distinguish among methane sources because a) fossil fuels are more depleted in $^{13}CH_4$ than are biogenic sources, and b) methane from manure lagoons is more enriched in $^{13}CH_4$ than methane from enteric fermentation is. Detecting isotopic methane is, however, very challenging because the isotopes are only present in small fractions. The atmospheric ratio of $^{13}CH_4$ to $^{12}CH_4$ is only about 1%. Other isotopes are present in even smaller amounts. For example, the natural abundance of deuterium is about 0.016%.

Table 1

Methane Sensing Considerations

Observations	Implications	Deficiencies
Emissions, especially in oil and gas industry can be dominated by episodic large leaks	Need high temporal cadence to see these episodic leaks	Satellite revisits and aircraft scheduling may result in weeks to months between measurements
Emissions are varied and worldwide	Need to sense all over the world at all times of the day	Absorption spectrometers, which sense reflected sunlight at 1.65 μm or 2.3 μm, have no capability at night and very limited capability over water and at high latitudes
For effective mitigation large leaks must be fixed rapidly	Near real-time processing may be desired	Retrieving methane concentrations from spectrometer measurements requires complex calculations that may take days to months
Where multiple sources of methane are present, there may be a need to distinguish isotopes	May require sensing proportions of isotopes: $^{12}CH_4$, $^{13}CH_4$, $^{14}CH_4$, $^{12}CH_3D$	Challenging to achieve sensitivity to sense isotopes that are present in only small fractions

1.3 THE NIFTY OPTICAL CONCEPT AND METHANE LEAK DETECTION

Although methane is a powerful greenhouse gas, its escape into the atmosphere from gas wells, pipelines, and local distribution networks is poorly monitored and disparately regulated worldwide. In addition to the environmental impact, there is significant revenue loss to energy companies from these leaks and loss mechanisms. Leak rates in the U.S. are estimated at between 1% and 2% overall, but are higher in the Permian Basin [10] and are much higher worldwide; it is estimated that existing leaks completely offset the greenhouse gas benefit of switching power generation plants from coal to natural gas [11]. Sensors capable of detecting methane leaks remotely with a high-area-coverage rate have an important role to play in identifying leaks so they can be mitigated.

Section 1.4 presents the sensitivity of a number of existing and planned sensors for methane leak detection. The existing sensors that offer high area coverage are necessarily passive and have limited sensitivity for leak detection. One of the reasons for the poor sensitivity is that the individual absorption lines of methane are spectrally very narrow (of the order of GHz) and widely separated, which means that typical imaging spectrometers with nm spectral resolution (~80 GHz in the SWIR) waste available SNR as they admit much more noise than signal in each spectral band. It is very difficult to build a wide-field-of view-spectroscopic imager with spectral resolution matched to the width of the absorption lines.

We developed an optical sensor designed to detect small gas molecules with MWIR absorption signatures at high sensitivity over wide fields of view. The concept, called NIFTy, uses an optical cell containing the gas to be detected in one arm of a path-matched, wide-field interferometer [12, 13]. This

arrangement creates a filter that is exactly matched to the narrow absorption lines of the gas, allowing passive detection at optimal SNR in an imaging mode.

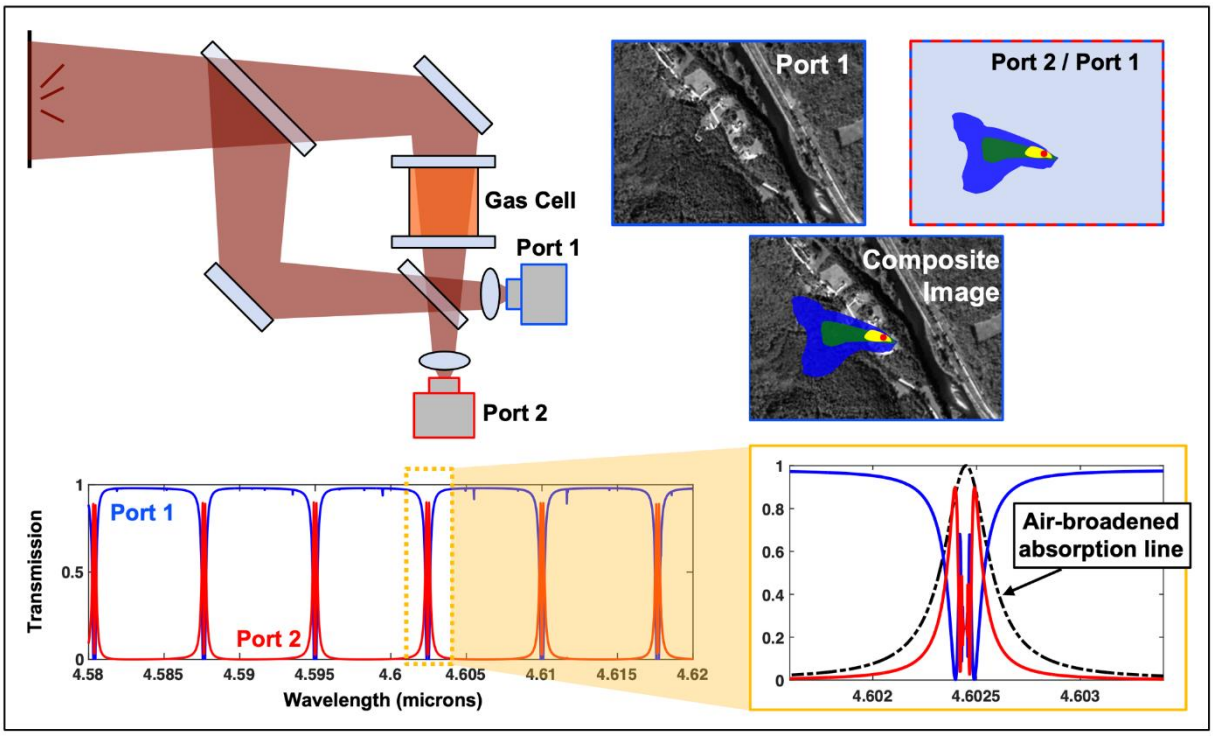

Figure 2. The NIFTy optical concept.

Figure 2 illustrates this optical system. The arrangement is a Mach-Zehnder interferometer. When the two arms are matched, the interference between the light from both arms of the interferometer at the second beam splitter causes all light from the scene to exit at port 1. If dispersion in the system is managed, this will be true across a wide optical bandwidth. Equally important, if the two arms are perfectly path-matched on-axis, they are path-matched at all field angles (provided certain optical requirements on the beam splitters are met), which means that the configuration will behave the same (spectrally) across a very wide field of view, and thus can be used as an imager. The effect of introducing the gas cell can be understood by recalling from Kramers-Kronig that an absorption resonance (a peak in the imaginary part of the electric susceptibility) must go along with a ripple in the real part of the susceptibility, which is proportional to the index of refraction. At wavelengths far from an absorption line, the index of refraction is unchanged and the cell does nothing. But near resonance, an additional path length is created, unbalancing the interferometer and sending just those wavelengths near resonance out the other port. Because the index of refraction goes above the value 1 (on the left of the absorption) and below 1 (on the right of the absorption), a double-humped passband is created at each absorption line. How wide those passbands are relative to the width of the air-broadened absorption linewidth can be adjusted by changing the pressure in the optical cell or adding a buffer gas.

The dark port of the interferometer will pass light only at wavelengths near the target-gas resonances, and the bright port will pass only the complementary wavelengths; this filter behavior is maintained across

a wide field of view. The change in the ratio of the power received at the two ports is a measure of the concentration of any intervening target gas that the light has passed through (similar to the measurement in differential absorption lidar, or DIAL [14]), and the number of lines across which the filter operates increases the specificity to that target gas and the SNR. Figure 2 shows a representative theoretical spectral transmission for the two output ports for a system optimized for the detection of carbon monoxide. Efficient transmission at more than ten absorption lines is possible, with very high rejection (>99%) between lines. The exact shape of the pass bands (the double peak and central null) comes from the derivative shape of the dielectric function, and the exact widths and heights are the result of optimizing the concentration of the target gas and buffer gas in the cell, such that the most light under the natural absorption width gets through while minimizing the out-of-band leakage.

The shape of the NIFTy filter as a function of target-gas physical parameters (line strength, line width, concentration, etc.) has been derived in a separate document [15], along with an optimization procedure. The theoretical model was experimentally validated with both carbon monoxide at 4.6 microns and with a separate interferometer using the near-infrared (NIR) overtone of acetylene.

The NIFTy concept was developed for detection of diatomic and triatomic species, where the isolated, widely separated absorption lines create the canonical wiggle in the index of refraction leading to isolated passbands through the interferometer. Methane (CH_4) has five atoms but significant symmetry, leading to absorption bands that are more complicated than that of a diatomic gas but that still maintain much of the same character. Therefore, this study was undertaken to determine if an efficient NIFTy sensor could be created using the strong 3.3 μm or 7.6 μm absorption bands, and if so, what would the expected performance be for remote methane leak detection. Our work has shown that a highly sensitive methane detection sensor can be built operating on the long-wavelength side of the 7.6 um absorption band, and that the expected performance could provide sensitivity to leaks rates as low as 1 kg/hr (per m/s of wind) at an area coverage rate around 740 km^2/hr. This NIFTy sensor would out-perform the best-in-class passive sensors currently operating. These design choices have been integrated into a notional sensor system that could fly on an uncrewed platform such as an MQ-9. We take advantage of newly available "dual-band" SLS (strained-layer superlattice) detectors that have sensitivity from the MWIR through LWIR to enable both methane sensing and also sensing of several gases of interest to the DoD/IC with absorption features in the MWIR. Such a system is described in Table 2, and compared to existing sensors in Section 1.4.

Table 2

Notional Sensor System Concept and Performance

Platform	MQ-9
FPA technology	1024x1024 SLS (2um-11um), 40 μm pitch
Optics	1.6" F/2.3
FOV	26°
GSD	2 m at 15,000'
Area coverage	740 km^2/hr
Sensitivity (at 15,000')	CH_4: 1 kg/hr (1°C ΔT) HCl: 11 grams/hr (daytime), 500 g/hr (night, 1°C ΔT) CO: 130 gram/hr (5°C ΔT) NO: ~ 1 kg/hr (5°C ΔT)

1.4 PERFORMANCE OF EXISTING METHANE SENSORS

A variety of sensors have been used for methane detection. Other sensors have been designed and will shortly come on line. Table 3 lists the characteristics of three spaceborne sensors and three airborne sensors and compares the calculated characteristics for an airborne NIFTy sensor [16,17,18]. The sensors are not meant to be a comprehensive list; they were chosen to give the "best-of-breed" for each type of sensor.

Table 3

Characteristics of Existing and Planned Methane Sensors (from [11-21])

Property	TROPOMI	MethaneSAT	Carbon Mapper	JPL	Bridger	SeekOps	*NIFTy*
Platform	Spaceborne	Spaceborne	Spaceborne	Airborne	Airborne	Airborne	*Airborne*
FOV	2,600 km	200 km	18 km	1.8-km swath ~360 sq-km/hr	128-m swath ~ 20 sq-km/hr	N/A	*2 km x 2 km 740 sq-km/hr*
IFOV	7 km x 7 km	130 m x 400 m	30-35 m	3 m x 3 m	~2 m	Point sensor	*2 m x 2 m*
Detection Threshold	12 ppb, 4,200 kg/hr	2 ppb, 100 kg/hr	50 – 150 kg/hr	5 – 10 kg/hr	< 3 kg/hr	10 ppb, 0.02 kg/hr	*1.0 kg/hr*
Altitude	824 km, sun sync	585 km, sun sync	400-410 km, sun sync	10,000 ft	~ 750 ft	Low—UAV dependent	*10,000 ft*
Sensors	Oxygen A (760 nm) & SWIR	2 SWIR spectrometers	Improved AVRIS	AVIRIS-NG spectrometer	Lidar	Absorption spectrometer	*NIFTy interferometer*
Funding	ESA	MethaneSAT LLC, Environmental Defense Fund	Carbon Mapper	NASA	Contract services	Contract services	*Line*
Developer	Airbus	Ball Aerospace, Blue Canyon	JPL, ASU, Planet	JPL	Bridger	SeekOps	*MIT/LL*
Status	Launched 13 October 2017	Launch fall 2023	Demo 2023, ~20 in 2025	Occasional flights	Operational	Operational	*To be demonstrated*

The three spaceborne systems all use imaging spectrometers operating in the SWIR. They differ principally in the choices each has made in overall area coverage and localization. TROPOMI has a very large field of view and an IFOV ~7 km [19]. MethaneSAT has a moderate coverage area and an IFOV of order 100 m [20]. Carbon Mapper has a smaller area coverage and an IFOV of ~30 m [21]. TROPOMI, because of its large coverage area, can only detect enormous leaks; its sensitivity is 4,200 kg/hr. MethaneSAT and Carbon Mapper are both supposed to have detection thresholds of ~100 kg/hr. This threshold is much better than TRPOMI's, but it is still within what is typically called the "super-emitter" range.

The three airborne sensors illustrate three different technologies. The JPL sensor is an imaging spectrometer, similar to the spaceborne systems [22, 23]. Because it is operating at much shorter range, however, it is able to get a sensitivity of ~10 kg/hr and to localize to ~3 m. The Bridger sensor is a lidar system; it achieves somewhat better sensitivity and localization than the imaging spectrometer, but lower coverage rate [24]. The SeekOps sensor is a point sensor; it achieves exquisite sensitivity but very low area coverage [25].

Table 4 shows the same seven sensors with a somewhat different list of properties. It includes the coverage, localization, and sensitivity from Table 3 but also includes other desirable features:

- Can the sensor work both day and night?
- Can the sensor work over water?
- Can the sensor provide real-time outputs?
- Can the sensor work at high temporal cadence?
- Can the sensor make continuous measurements?
- Can the sensor make measurements of methane isotopes?

Table 4 scores the sensors using a qualitative color coding of red/orange/yellow/green/ blue, where red is the worst and blue is the best. We can draw a number of conclusions from Table 4.

- First, each of the six existing and planned sensors has at least one property scored as red.
- Second, there is an obvious tradeoff between coverage and sensor performance. TROPOMI achieves global coverage, but otherwise does not score well. At the other end of the spectrum, SeekOps has some of the best sensitivity and localization, but the poorest coverage area. Other sensors, for instance Carbon Mapper or the JPL sensor, make different tradeoffs between performance and coverage.
- Finally, the proposed NIFTy sensor scores overall better than the other sensors. It achieves sensitivity and localization comparable to the SeekOps system, but with much better area coverage. It is able to operate day or night, work over water, and provide near-real-time information—things that are impossible or very limited from the other systems. It appears that NIFTy may even be capable of some sensing of methane isotopes.

Table 4

Scoring for Existing and Planned Methane Sensors

Scoring is on a qualitative color scale of red/orange/yellow/green/blue, where red is the worst performance and blue is the best.

Property	TROPOMI	MethaneSAT	Carbon Mapper	JPL	Bridger	SeekOps	NIFTy
Platform	Spaceborne	Spaceborne	Spaceborne	Airborne	Airborne	Airborne	Airborne
Coverage	Global	Regional	Large area	Moderate area	Local	Local	Moderate area
Localization	7 km x 7 km	130 m x 400 m	30-35 m	~3 m	~2 m	Point sensor	2 m
Sensitivity	~4,000 kg/hr	~100 kg/hr	~150 kg/hr	5– 10 kg/hr	~3 kg/hr	~0.02 kg/hr	<1.0 kg/hr
Day/Night?	No	No	No	No	Possible	Possible	Yes—LWIR
Over-Water?	Very limited	Very limited	Very limited	Very limited	Possible	Demonstrated	Yes—LWIR
Near Real Time?	Multiple passes, retrieval	Days	Days	Days?	Hours	Hours	Yes
Cadence?	Satellite repeat	Satellite repeat	1-7 days with constellation	Daily, in principle	Daily, in principle	UAV logistics?	Platform dependent
Continuous Measurements?	Satellite pass time	Satellite pass time	Satellite pass time	Over modest regions	Small aircraft limited	Very small area	Platform dependent
Isotope Measurement?	Too insensitive	Too insensitive	Too insensitive	Unlikely	Unknown	Sensor change required	$^{13}CH_4$ possible

Figure 3 compares the various methane sensors in a different format. We plot minimum detectable leak rate versus area coverage rate for the six best-in-class sensors, as well as for the proposed NIFTy sensor. Not surprisingly, the plot shows a strong tradeoff between sensitivity and area-coverage rate. Interestingly, the six best-in-class sensors all fall on a line given by the relation

Minimum Detectable Leak Rate $\propto$ (Area Coverage Rate)$^{0.65}$.

The proposed NIFTy sensor follows the same relationship but with a roughly 10x improvement from the trend line of the other six sensor.

Figure 3 shows the leak rate commonly accepted as that of a "super emitter." We see that only the airborne sensors can measure emission below that of a super emitter. The sensitivity of spaceborne systems puts them well into the range of super emitters.

Also shown in Figure 3 is a band defined by the newly proposed EPA standards for required remediation [26]. The lower limit of this band is for a continuous emitter; the upper limit is for an emitter with 10% duty cycle. We see that the SeekOps sensor clearly supports the new EPA standard but with very low coverage rate. The Bridger and JPL systems barely get into the band for the new standard. The proposed NIFTy system gets solidly in the range of the new EPA standard with reasonable area coverage. To give context to the area coverage, Figure 3 shows that an area coverage rate of 1,000 km^2/hr would enable sensing the entire 2.2 million acre Chevron holdings in the Permian basin in only 9 hours.

Thus, in comparing NIFTy to other existing and planned sensors, we find that NIFTy breaks the prevailing trend line to provide about an order of magnitude improvement in performance. NIFTy should provide a unique combination of a) standoff sensing with reasonable area coverage and b) sensitivity required to support the new proposed EPA leak-remediation requirements.

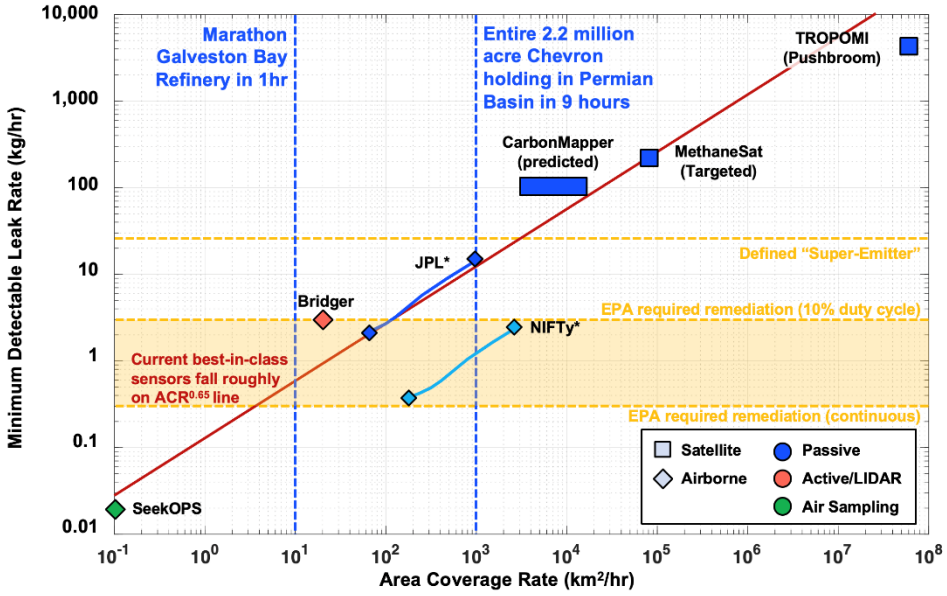

Figure 3. Minimum detectable leak rate versus area coverage rate for airborne and spaceborne sensors.

2. NIFTY SENSOR FOR METHANE LEAK DETECTION

2.1 OVERVIEW AND STUDY APPROACH

When used in the NIFTy interferometer, the isolated absorption lines in a diatomic gas such as carbon monoxide result in isolated, narrow (albeit double-humped) passbands previously shown in Figure 2. The MWIR and LWIR absorption features of methane are more complicated, and therefore it is unclear how effective the filters resulting from using methane in the NIFTy configuration would be for high-sensitivity and high-specificity detection. In addition, the strength of the methane absorption resonances is not as high as that for typical diatomic gases, and so the interplay between the gas concentration, cell length, and pressure broadening needs to be carefully modeled. Figure 4 shows the difference between the 4.6 µm vibrational band of carbon monoxide and the 7.6 µm band of methane. The goal of this part of the Methane Study was to answer the question: Can the NIFTy optical design be applied to detection of methane natural gas leaks, and if so, what would the sensor look like and what would the predicted performance be?

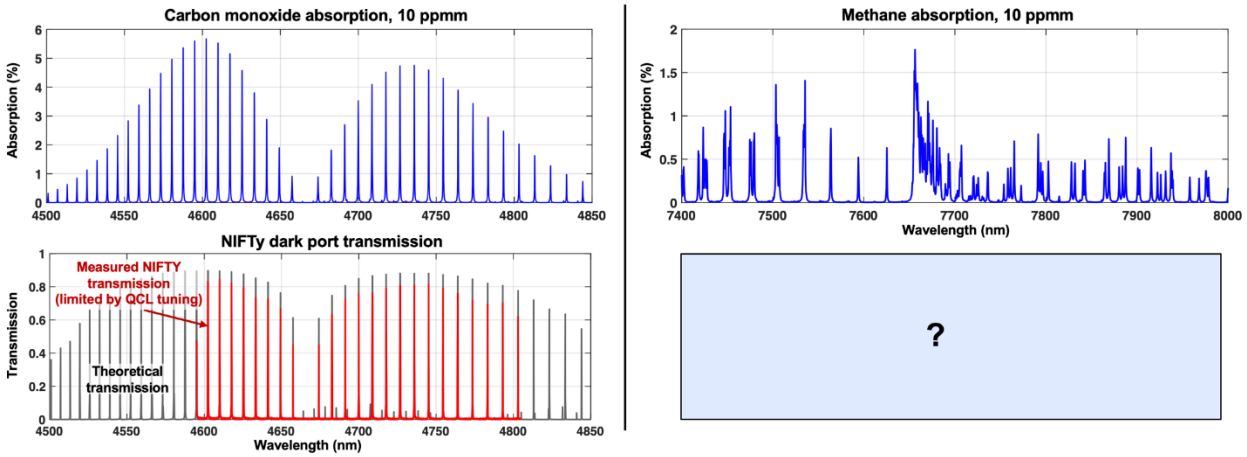

Figure 4. Carbon monoxide and methane absorption bands and resulting NIFTy filter.

To answer these questions, we first developed a formalism to express the sensitivity of an idealized passive spectroscopic sensor based on the physical properties of the gas under study and modeled upwelling ground and path spectral radiance, along with noise from the detector and warm optics. This enabled the comparison of a NIFTy sensor operating at either of the two IR bands with an ideal imaging spectrometer operating in the SWIR for comparison. This analysis showed that the 7.6 µm band would provide significantly higher sensitivity than the 3.3 µm band, and would also be competitive with a SWIR hyperspectral imager that had an exceedingly high spectral resolution, matched to the width of the individual absorption lines (a sensor that is beyond state of the art). Second, the fidelity of this model was

extended to include the actual spectral shape of the NIFTy filters to provide an accurate estimate of the SNR-limited detection sensitivity and allow optimization of all sensor parameters (exact spectral band, gas cell parameters, etc.). Finally, computational fluid dynamics models of release plumes were developed to allow the relationship between sensor performance, measured in concentration-length product (minimum detectable quantity or MDQ) with the gas release rate, measured in kg/hr.

2.2 ESTIMATION OF IDEAL PERFORMANCE

Figure 5 shows the transmission of a typical atmosphere in blue with the absorption of 1,000 ppm-m of methane in red. The strongest IR-active bands are the ν_3(F2) stretch at around 3.3 µm and the ν_4(F2) bend mode around 7.6 µm. The much weaker ν_1 band is visible around 2.3 µm, along with the $2\nu_3$ overtone around 1.6 µm. Despite the weak absorption strength, most spectroscopic remote sensing of methane is done at one of the two SWIR bands, to take advantage of lower noise detectors and avoid thermal noise, and because the atmosphere is much more benign there. (Atmospheric water near the 3 µm edge of the MWIR transparency region and near the 8 µm edge of the LWIR region both attenuate the ground radiance and complicate quantification.) However, looking at the individual lines of the MWIR and LWIR bands reveals that there are many individual absorption lines that are located between the water and other interferents, and therefore operating in the MWIR or LWIR could allow more sensitive methane detection if sufficient spectral resolution could be obtained. This is the premise of the NIFTy methane study.

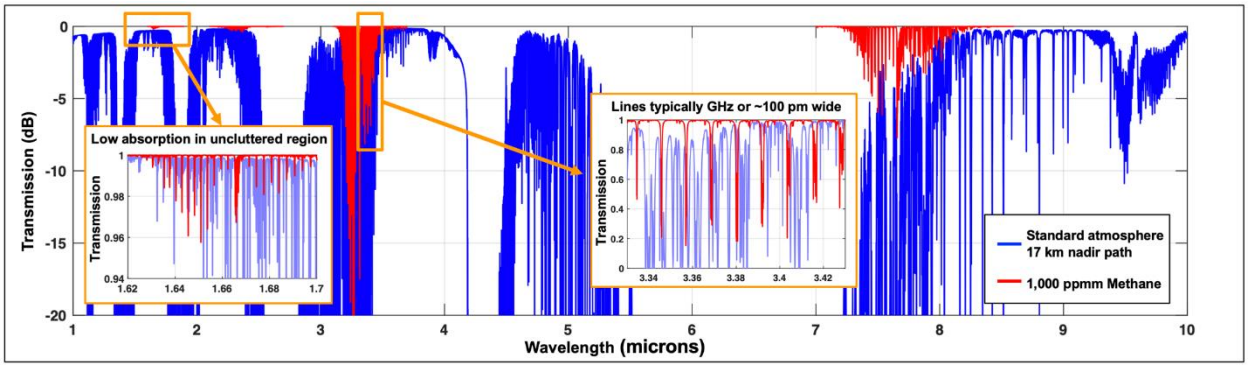

Figure 5. Methane absorption bands and atmospheric transparency.

Both the ν_3 and ν_4 modes have sufficient absorption strength that a NIFTy filter could be created with reasonable cell gas pressure and length. (If the absorption strength of each line is too weak, the cell would need to be so long as to severely limit the field of view of the sensor; gas pressure cannot be increased to allow for a shorter cell because of the effects of pressure broadening.) The first task of the study was then to identify at which of the two bands would a NIFTy-based sensor perform better, and how would such a sensor compare to an ideal spectrometer operating on the SWIR.

To estimate the performance of a NIFTy sensor in a manner that allows direct comparison with spectroscopic sensors, we first write the estimator for the NIFTy detection approach, derived in a separate document [15]. For a pixel with $n^{(1)}$ photoelectrons detected through the wideband port and $n^{(2)}$ photoelectrons detected through the narrow passband port, the concentration-length product estimate can be written,*

$$CL = CL_0\left\{ln\left(\frac{n^{(1)}}{n^{(2)}}\right) - ln\left(\frac{n_{OFF}^{(1)}}{n_{OFF}^{(2)}}\right)\right\} \quad 2.1$$

where $n_{OFF}^{(1)}/n_{OFF}^{(2)}$ is the average of the ratio in the absence of any target gas (that is, the background level that must be subtracted from the estimate). As we are considering the case of an on-plume pixel, we write

$$= CL_0\left\{ln\left(\frac{n_{ON}^{(1)}n_{OFF}^{(2)}}{n_{ON}^{(2)}n_{OFF}^{(1)}}\right)\right\} \quad 2.2$$

which, as the photoelectron count at the wideband port is hardly changed by the presence of the gas, is approximately equal to $CL_0 ln(n_{OFF}^{(2)}/n_{ON}^{(2)})$. This makes sense and follows from Beer's Law: for a passband roughly equal to the width of an absorption line, the change in transmission is proportional to $exp(-\alpha\ell)$, and so the concentration-length product, that is, $\alpha\ell$, is proportional to the logarithm of the in-band ratio. The scale factor CL_0 would be measured in the lab, but for modeling purposes, it can be calculated from the radiance and absorption and emission of the target at a given ground-plume temperature difference:

$$CL_0 = \frac{\Delta}{\Delta CL}\left\{ln\left(\frac{n_{ON}^{(1)}n_{OFF}^{(2)}}{n_{ON}^{(2)}n_{OFF}^{(1)}}\right)\right\} \sim \left\{ln\left(\frac{n_0^{(2)}}{n_{1ppmm}^{(2)}}\right)\right\}^{-1} ppmm \quad 2.3$$

The estimator can then be written as a function of four variables:

$$CL = CL_0 \times f, where\ f\left(n_{ON}^{(2)}, n_{OFF}^{(2)}, n_{ON}^{(1)}, n_{OFF}^{(1)}\right) = ln\left(\frac{n_{ON}^{(1)}n_{OFF}^{(2)}}{n_{ON}^{(2)}n_{OFF}^{(1)}}\right) \quad 2.4$$

* In practice, the inverse ratios are calculated ($n^{(2)}/n^{(1)}$) to avoid small numbers in the denominator; this simply changes the sign of the logarithm.

Using standard error propagation, we can write the variance of the estimator

$$\sigma^2(CL) = {CL_0}^2 \left\{ \left(\frac{\partial}{\partial n_{ON}^{(2)}} f \right)^2 \sigma^2\left(n_{ON}^{(2)}\right) + \left(\frac{\partial}{\partial n_{OFF}^{(2)}} f \right)^2 \sigma^2\left(n_{OFF}^{(2)}\right) \right. \tag{2.5}$$

$$\left. + \left(\frac{\partial}{\partial n_{ON}^{(1)}} f \right)^2 \sigma^2\left(n_{ON}^{(1)}\right) + \left(\frac{\partial}{\partial n_{OFF}^{(1)}} f \right)^2 \sigma^2\left(n_{OFF}^{(1)}\right) \right\}$$

$$\sigma^2(CL) = {CL_0}^2 \left\{ \frac{\sigma^2\left(n_{ON}^{(2)}\right)}{\left(n_{ON}^{(2)}\right)^2} + \frac{\sigma^2\left(n_{OFF}^{(2)}\right)}{\left(n_{OFF}^{(2)}\right)^2} + \frac{\sigma^2\left(n_{ON}^{(1)}\right)}{\left(n_{ON}^{(1)}\right)^2} + \frac{\sigma^2\left(n_{OFF}^{(1)}\right)}{\left(n_{OFF}^{(1)}\right)^2} \right\} \tag{2.6}$$

$$\sigma^2(CL) \sim 2 \times {CL_0}^2 \left\{ \frac{\sigma^2\left(n^{(2)}\right)}{\left(n^{(2)}\right)^2} \right\} \tag{2.7}$$

The wideband port (1) transmits more than 30 times as much light as the narrowband port, so the $n^{(1)}$ terms can be ignored as they will not significantly change the SNR. The two narrowband port (2) terms are roughly the same magnitude and so can be combined leading to the factor of two in front, although as the OFF values could likely be averaged over many pixels, this is conservative. Equation 2.7 says that the variance in our concentration-length estimate varies inversely with the SNR^2, where the SNR is determined primarily by the narrowband port photoelectron count, which is the expected result.

The SNR can be written in terms of the photoelectron flux $\dot{n}$ and Γ_{BCR}, the background count rate, which is the sum of the detector dark current, thermal flux from the optics, and path radiance.

$$SNR^2 = \frac{(\dot{n}T)^2}{\dot{n}T + \Gamma_{BCR}T} \tag{2.8}$$

Dividing by the measurement time gives a metric independent of integration time

$$SNR^2/T = \frac{\dot{n}^2}{\dot{n} + \Gamma_{BCR}} \tag{2.9}$$

which allows the concentration-length variance to be expressed also independent of integration time.

$$\sigma^2(CL)T \sim (2) \times {CL_0}^2 \left\{\frac{1}{SNR^2/T}\right\} \quad 2.10$$

$$MDQ = \left(\sqrt{2}\right) \times CL_0 \frac{1}{\sqrt{SNR^2/T}} \quad 2.11$$

The minimum detectable quantity, or MDQ, is proportional to the modulation effected by a certain quantity of gas at a given ground-plume temperature difference, and inversely proportional to the SNR, and has units of ppm-m°C/Hz$^{1/2}$. What remains is to determine the received photoelectron count.

As we are considering down-looking airborne or space-based remote sensing, this analysis begins with a model of the ground spectral radiance. This is a combination of the reflected solar radiation and the thermal emission from the ground itself, and is described by Equation 2.12.

$$\mathcal{L}_g(\nu) = I_{solar}(\nu)\tau_{s-g}(\nu)\mathcal{R}_g \frac{1}{\pi} + \varepsilon B\left(\nu, T_g\right) \quad 2.12$$

To model the solar component, the exoatmospheric solar radiance [27], interpolated onto a 100 MHz grid spacing, is propagated through a high-spectral-resolution model of the atmosphere generated with MODTRAN 6 using the "line-by-line" feature to accurately capture the 100 MHz detail (space-to-ground, 45° mid-latitude summer). This is then multiplied by an average 20% ground reflectivity and uniformly spread over π steradians. The ground thermal emission is simply the Planck function at T = 300K times an average emissivity of 1. A spectrally varying reflectivity or emissivity may be more accurate, but this model is sufficient for this initial study.

Figure 6 shows this function across the entire SWIR/MWIR/LWIR optical band, with a red dot placed at the exact spectral radiance value at each of the many individual methane absorption lines. In the SWIR, there is significant solar radiation at each line position. At the 3.3 μm ν_3 band, the strong absorption of the roughly 1 ppm atmospheric background of methane, integrated through the entire atmosphere, absorbs virtually all the incident solar radiation so that the upwelling radiance exactly at each methane line is solely from the thermal ground emission, which at 3.3 microns is rather low. At the 7.6 μm ν_4 band, where ground emission dominates the solar reflection, the radiance is high but the exact received signal will depend on the altitude of the receiver platform, because the absorption from the background atmospheric methane will attenuate the upwelling radiance with increasing sensor altitude.

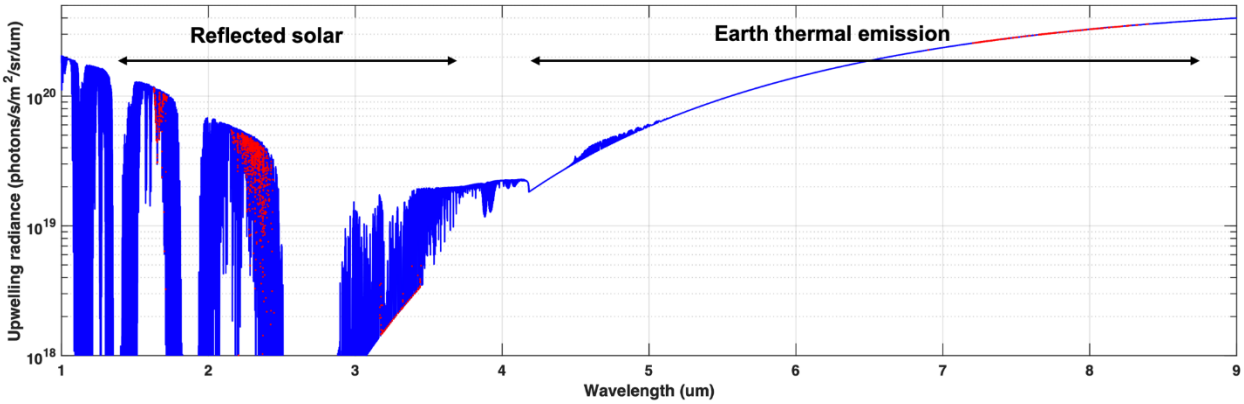

Figure 6. Modeled ground spectral radiance.

The upwelling ground spectral radiance is combined with a three-layer plume model [28] to obtain the source terms. In the three-layer plume model, the at-aperture radiance is calculated for a ground sample where light has propagated through the target gas ("on" the plume) and for a ground sample where no plume is present ("off" plume). The at-aperture radiance off-plume is the upwelling ground radiance times the atmospheric transmission plus the atmospheric path radiance. For the on-plume radiance, the upwelling ground radiance also passes through the plume, and there is an additional term from the emission of the plume itself.

$$\mathcal{L}_{OFF}(\nu) = \mathcal{L}_g(\nu)\,\tau_{atm}(\nu) + \mathcal{L}_{path}(\nu)$$

$$\mathcal{L}_{ON}(\nu) = \mathcal{L}_g(\nu)\,\tau_{plume}(\nu)\,\tau_{atm}(\nu) + \mathcal{L}_{plume}(\nu)\,\tau_{atm}(\nu) + \mathcal{L}_{path}(\nu)$$

$$\tau_{plume}(\nu) = exp\left\{-\sum\nolimits_i \alpha_i \ell\right\} \qquad 2.13$$

$$\mathcal{L}_{plume}(\nu) = \left(1 - exp\left\{-\sum\nolimits_i \alpha_i \ell\right\}\right) B\left(\nu, T_{plume}\right)$$

$$\alpha_i \ell = \frac{S_i}{\pi} \frac{\Gamma_i}{(\nu - \nu_0)^2 + \Gamma_i^2} \times n_{plume} \ell$$

The ground-to-sensor atmospheric transmission τ_{atm} and path radiance $\mathcal{L}_{path}$ are obtained from ModTran runs at a range of sensor altitudes. The plume transmission is simply the exponential of the sum of Lorentzians with line parameters taken from the HITRAN database, and the plume radiance is given by the Planck blackbody function $B\left(\nu, T_{plume}\right)$ times the plume spectral emissivity, which is one minus the transmission. Note that the ground-plume temperature difference is a critical input. The contrast is zero

for a temperature difference of zero and increases linearly with the absolute value of the temperature difference.

From the on- and off-plume radiances, we can write an expression for (and calculate) the photoelectron counts rates

$$\dot{n}_{OFF}^{(1)} = \eta_{sys} \int \mathcal{L}_{OFF}(\nu)\, F^{(1)}(\nu) d\nu \times A\Omega$$

$$\dot{n}_{ON}^{(1)} = \eta_{sys} \int \mathcal{L}_{ON}(\nu)\, F^{(1)}(\nu) d\nu \times A\Omega$$

$$\dot{n}_{OFF}^{(2)} = \eta_{sys} \int \mathcal{L}_{OFF}(\nu)\, F^{(2)}(\nu) d\nu \times A\Omega \qquad 2.14$$

$$\dot{n}_{ON}^{(2)} = \eta_{sys} \int \mathcal{L}_{ON}(\nu)\, F^{(2)}(\nu) d\nu \times A\Omega$$

$$\text{where } A\Omega = \frac{\pi}{4}\frac{d_{pix}^2}{F\#^2} \; or = \frac{\pi}{4}\lambda^2$$

and η_{sys} is the optical efficiency through the sensor including detector quantum efficiency. $F^{(1)}$ and $F^{(2)}$ are the spectral shapes of the wideband and narrowband transmission functions derived in [15].

This formalism is useful because Equation 2.2 is also the estimator for an ideal spectrometer. That is, this equation expresses the best possible (clutter-free) performance that could be obtained from a spectrometer where the spectral resolution is matched to the spectral width of the absorption lines of the species being measured. Therefore, as an initial comparison, this formalism was applied to determine the MDQ for detection of methane at all four infrared bands, varying the total passband used. For this initial study, a binary filter functions $F^{(2)}$ was used, with transmission of 1 within the full width at half-maximum (FWHM) of each absorption line and zero everywhere else. The wideband filter $F^{(1)}$ is not required for this analysis. The results at 3 microns and 7.5 microns apply to a NIFTy sensor, as we have shown that an efficient NIFTy filter can be created with a reasonable cell length at these wavelengths. The results at 1600 nm and 2300 nm represent optimal performance for a SWIR spectrometer. Parameters for the analysis are summarized in Table 5, and results for a 5,000-foot sensor altitude are presented in Figure 7.

Table 5

Noise Parameters Used in Simulation

	1.65 µm	2.4 µm	3.3 µm	4.6 µm	7.8 µm
Principal noise source	Detector dark current	Detector dark current	Detector and optics	Emission from optics	Emission from optics
Value used	$1x10^5$ e^-	$1x10^5$ e^-	$1.2x10^{-6}$ e^-/Hz	$4x10^{-5}$ e^-/Hz	$7.2x10^{-4}$ e^-/Hz
Method	Literature	Literature	Planck function	Measured	Planck function

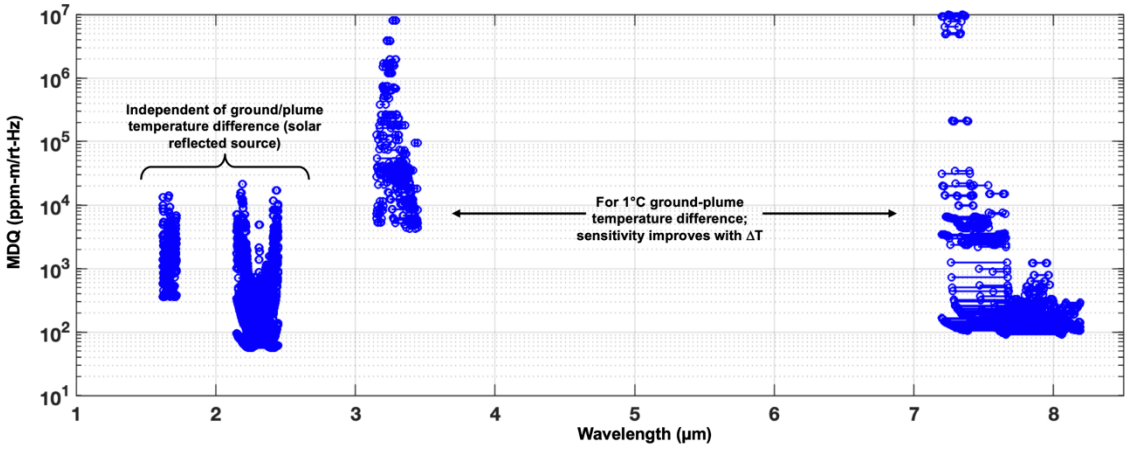

Figure 7. Performance of a MWIR/LWIR NIFTy sensor compared to ideal SWIR spectrometer.

Although the absorption strengths of the MWIR and LWIR lines are comparable, the very low ground radiance at the MWIR lines, because the solar illumination is absorbed and the ground thermal emission is low, results in poor performance for a NIFTy sensor operating in the MWIR. The strong ground radiance in the 7-8 µm region, however, predicts high-sensitivity performance with an MDQ as low as 100 ppm-m°C/$Hz^{1/2}$. This is comparable to the best possible SWIR spectrometer, noting that such an ideal spectrometer with a ~50 pm spectral resolution does not exist. The SWIR spectrometers are also necessarily daytime only, as there is no ground thermal emission at these short wavelengths. The day/night capability, at a sensitivity comparable to the theoretical best performance of a SWIR sensor, suggests that a LWIR NIFTy methane sensor could provide a significant improvement over state of the art.

2.3 HIGH-FIDELITY SENSITIVITY MODELING

Having identified with a simplified model that the LWIR band is worth further analysis, a more complete, end-to-end simulation was developed. For simplicity, the above analysis assumed a "perfect" NIFTy filter with unity transmission at each absorption line, and zero elsewhere, but this leaves out the impact of out-of-band light reaching the narrowband port (2) focal plane, and in-band light reaching the port (1) focal plane, which changes both the sensitivity scaling (the CL_0-term) and the impact of the atmospheric radiance noise on the SNR. The true shape of the NIFTy filter must be included, and the CL_0 scaling must be calculated accurately using that filter shape.

We have previously shown that the shape of the NIFTy filter can be accurately predicted at a MHz frequency resolution from gas parameters from the HITRAN database and knowledge of the gas cell length and concentration of target gas and any other gas in the cell [29]. Figure 8 shows the typical NIFTy filter shape for widely separated, isolated absorption lines of the diatomic molecule carbon monoxide, the target studied in the 2021 and 2022 Optical Systems and Technology Line Airborne Phenomenology effort. A double-humped transmission peak occurs under every ro-vibrational line, with about 80-90% peak transmission. The model prediction matches the laser-based transmission measurement very well.

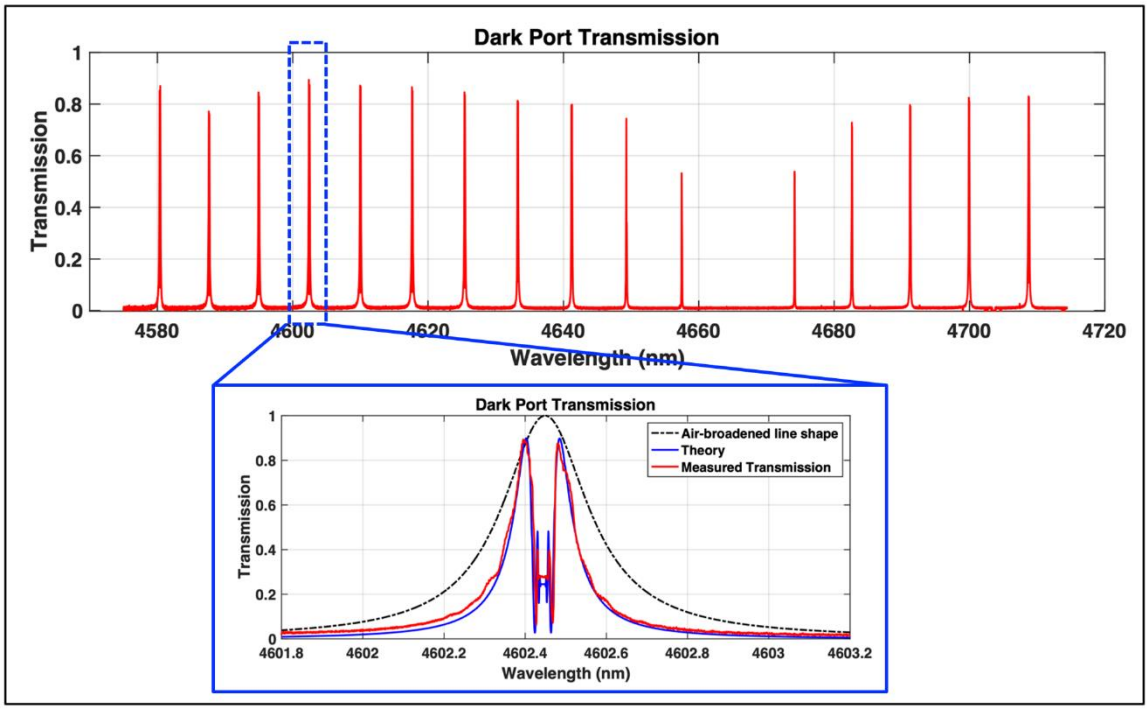

Figure 8. Measured and modeled NIFTy passband spectra for CO.

Using this established code, the filter shape for a methane NIFTy sensor can be predicted in the same way. The cell length and methane concentration parameters were varied and optimized using the predicted MDQ of the sensor that results as an optimization metric. Figure 9 shows the transmission spectrum of the NIFTy spectrometer with this optimized methane cell, with length 15 cm and 30 torr of methane. For the majority of the lines, a high-transmission passband is created with good between-band rejection, even where the lines are close together. In the shorter-wavelength region, where many lines overlap, the filter shape becomes less ideal as the passband transmission comes down, and the between-band rejections rises, for example, near 7.71 μm. Although this behavior is not ideal, all the effects are included in the optimization method and so the resulting filter is the best available in a detection-sensitivity sense. Note that the increase in the between-band transmission could also lead to a decrease in the specificity of the sensor, or increase sensitivity to clutter from other gases. These effects have not yet been taken into account in the analysis.

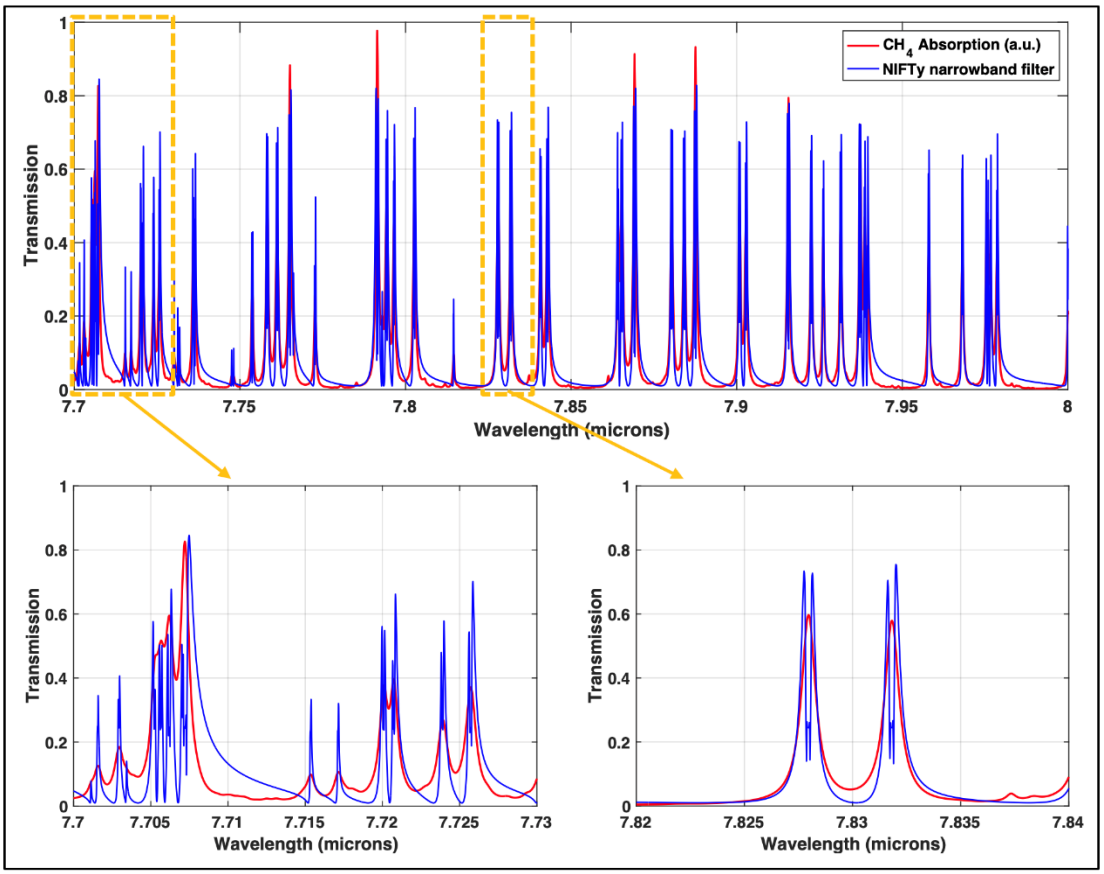

Figure 9. Example NIFTy narrowband spectrum (15 cm, 30 torr cell).

Rather than calculate the sensitivity scaling (the CL_0 term) assuming a perfect binary filter, once we have the predicted shape of the NIFTy filter based on gas cell parameters, it is possible to calculate the actual MDQ by simulating many detection realizations using appropriate photoelectron statistics. Figure 10 summarizes the entire simulation. As before, a model of the ground radiance and ModTran are used to calculate the at-aperture radiance (both ground and path) that the sensor would see at any altitude for a pixel both on- and off-plume, using the three-layer model with a given concentration-length product for the plume layer. These spectral radiances are then multiplied by the NIFTy filter functions (wideband and narrowband filters) for a chosen set of gas cell parameters. The spectral flux is also sent through a cold filter whose center wavelength and bandwidth can also be varied and optimized. The resulting spectral radiances can then be summed across the cold-filter band, as the detector would, to yield four quantities: the photoelectron count on and off the plume, at the wideband and narrowband camera ports. With these four quantities, 10,000 Poisson realizations of the concentration-length estimate are computed, allowing an SNR to be estimated for this particular concentration-length product (and ground-plume temperature difference, and integration time). This entire process is repeated at a range of concentration-length products, producing a linear SNR versus concentration-length product graph. The MDQ is identified by interpolating this sampled function at an SNR of 3. In this manner, a wide range of sensor parameters and flight profiles or environments can be varied and their impacts understood.

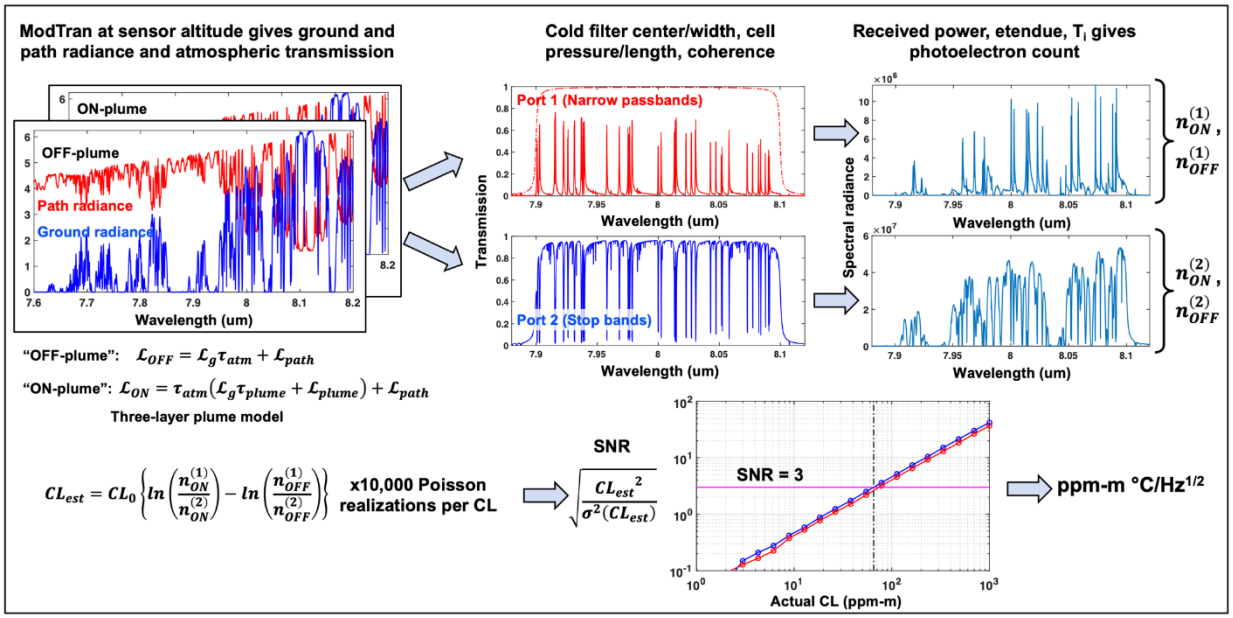

Figure 10. Simulation method.

Once a range of cell parameters (length and concentration) have been determined that produce an effective filter, the next important parameters to identify are the center wavelength and cold filter bandwidth that will provide the best MDQ. If every methane absorption line had equal strength and were equally spaced, then a wider bandwidth would always increase SNR, as the signal (amount of light through the passbands) increases linearly with bandwidth and the noise (the between-band light that leaks through the narrowband filter from the warm optics or the scene) only increases as the square root. It is the variable spacing and absorption strength of the various lines, then, that creates an optimal bandwidth less wide than the full absorption band. As an example, Figure 11 shows how the MDQ decreases with increasing cold filter bandwidth until about 500 nm, when centered at 7.9 µm, and then begins to rise again as the noise begins to outpace the increase in signal. This particular example, a 490 nm passband at 7.9 µm, has been determined to be the optimal objective system design point. As the platform altitude is increased, the background abundance of methane in the atmosphere attenuates the incident light, increasing the MDQ. As Figure 12 shows, this increase rolls over at a platform altitude of around 50,000 feet. Although the ~12x decrease in sensitivity from 5,000 feet to 50,000 feet and above is significant, the results do suggest that a space-based platform would still retain capability for detecting and localizing larger leaks.

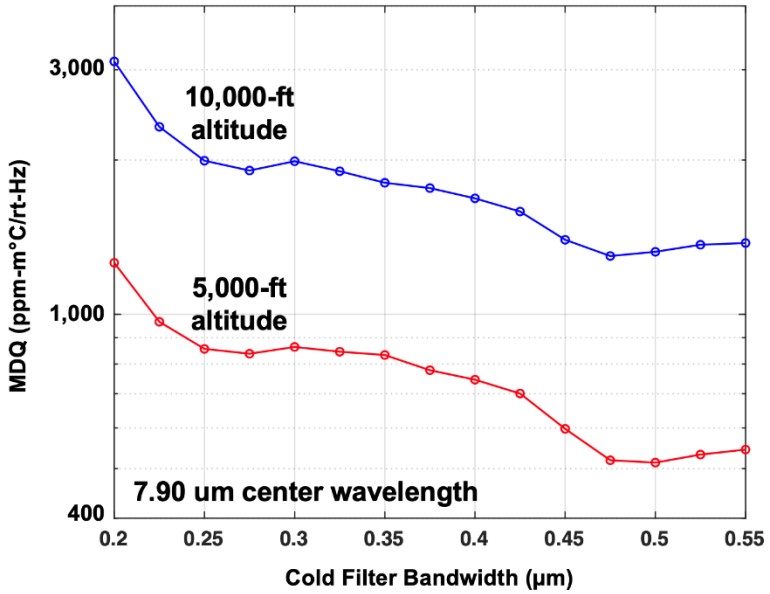

Figure 11. Variation of MDQ with cold filter bandwidth.

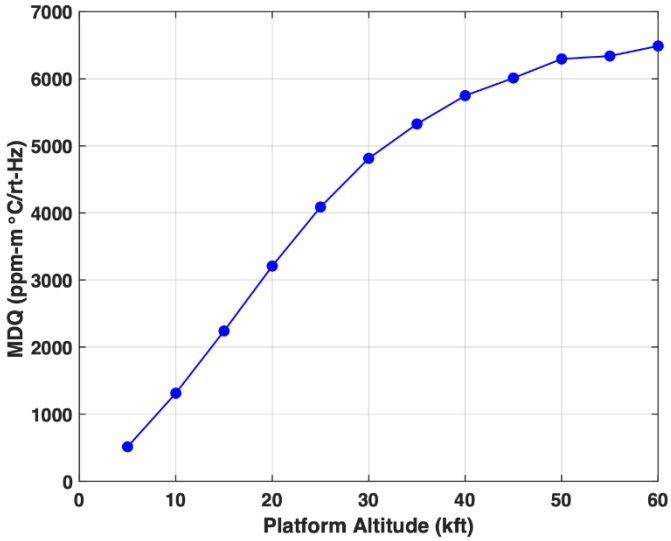

Figure 12. Increase in MDQ with platform altitude.

The formalism and analysis presented has identified that a NIFTy sensor operating at the 7.6 µm band of methane would have high sensitivity and could be built within reasonable SWaP. The cell length would need to be 15 cm, which makes the interferometer slightly larger than the version built for carbon monoxide, but still in the same size range. The optimal band to admit (the cold filter location) is 490 nm centered at 7.9 µm. Assuming the principal noise sources are from the path radiance and thermal emission from the optics, the sensitivity at 5,000 feet is predicted to be roughly 500 ppm-m°C/Hz$^{1/2}$, and about twice that at 10,000 feet. In order to determine a corresponding minimum detectable methane leak rate, we must understand how plumes disperse into the atmosphere.

2.4 METHANE PLUME MODELING

2.4.1 Problem Statement

The sensitivity figure of merit for all passive optical remote chemical sensing systems is the minimum detectable quantity expressed as some variation on a concentration-length product. The smallest detectable modulation in the incident optical signal corresponds to a smallest detectable quantity of the chemical in question; it does not matter if there is a short length of a high concentration or a long path through a low concentration. A common unit is parts per million meter (ppm-m), usually per-root-Hertz to capture the increase in sensitivity with integration time, and with a °C when considering MWIR or LWIR sensors where the thermal emission from the ground is the light source and the optical modulation increases with ground-plume temperature difference. However, for leak detection, the figure of merit is the minimum detectable leak rate, usually expressed in kg/hr, m^3/hr, or sometimes standard cubic feet per minute (SCFM). In order to get from a sensor MDQ to a system minimum detectable leak rate, the behavior of the gas plume created

from a leak, specifically the three-dimension distribution of the concentration that develops, must be understood.

To this end, an extensive plume-modeling study was undertaken with the goal of generating representative three-dimensional clouds at high spatial sampling so that the two-dimensional spatial distribution of concentration-length product that a down-looking sensor would observe could be understood and then used to relate ppm-m to kg/hr. Figure 13 shows this approach. A 3D plume simulated at a specific release rate is integrated in the vertical direction yielding a high-resolution map of concentration length (CL). Then the concentration length product at the release point is averaged across ground-sample distances (GSDs) of increasing size, providing the peak CL that would be measured verses the sensor GSD. As the concentration length varies inversely with wind speed (see Section 2.4.6), this provides the release rate per m/s of wind speed that would generate a given peak CL (the ratio highlighted in orange). The minimum detectable release rate (MDRR) can then be estimated by multiplying this ratio by the MDQ and the integration time, which is set by the platform velocity (v_p) and the number of pixels in the along-track direction $N_{pix}^{\parallel}$.

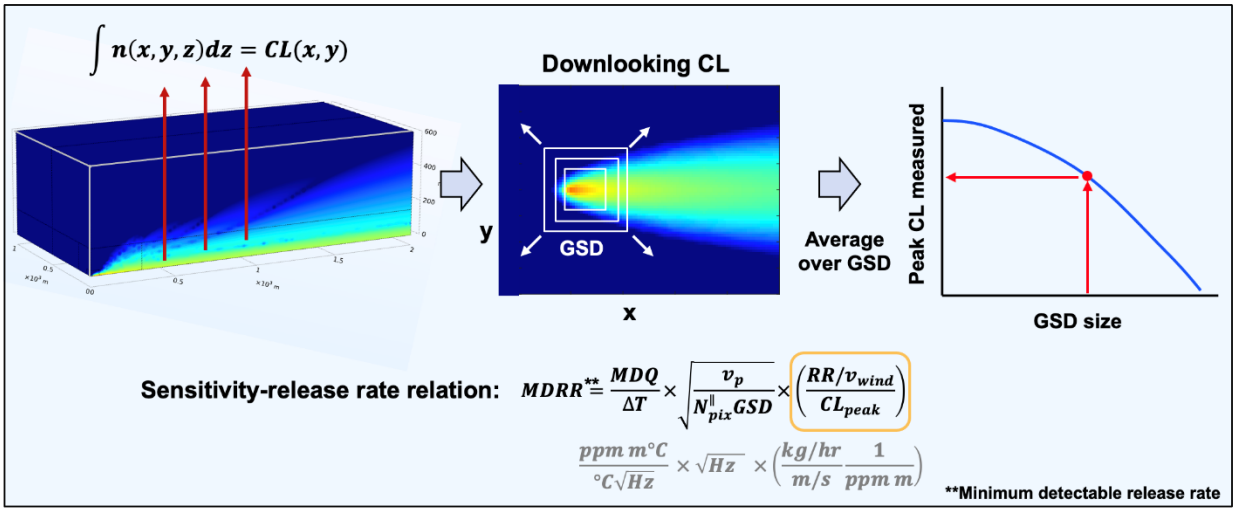

Figure 13. Approach for relating MDQ to minimum detectable release rate.

Simulations of methane plume formation were created using COMSOL Multiphysics. The simulation involved constructing a 3D representation of a methane plume by taking into account various parameters affecting plume formation such as windspeed, ambient wind temperature, and local geometry of the methane leak source.

2.4.2 Simulation Setup and Boundary Conditions

COMSOL is a commercial turnkey finite-element modeling package capable of simulating multiple coupled physics. In this work, the computational fluid dynamics (CFD) module and transport of concentrated chemical species (TCS) modules were coupled together to simulate the spreading and flow of methane gas from a concentrated leak source. The leak source was placed in an ambient outdoor environment, operating at steady-state conditions. Once set up, the simulation outputs all the relevant physical quantities, such as velocity, local chemical concentration, and pressure.

The CFD model selected was the k-ω turbulence model, which is a computationally intensive but accurate model useful for complex flows, such as jet flows. It was assumed that a constant methane leak from a pressurized system would mimic a jet flow, hence the selection of the k-ω turbulence model. The model, which solves for the turbulence kinetic energy (k) and specific rate of dissipation energy (ω), is well known in the literature. The disadvantages of using the k-ω model are the aforementioned computational requirements and lowered robustness to reach convergence without a good initial guess and careful element meshing design. These required the use of load-ramping strategies and mesh-refinement strategies to reach convergence in this work.

The chemical-species module uses a mass-conservation equation to track the flow of chemical species throughout a simulation domain. Mass diffusion is calculated using a mixture-averaged Fick's diffusion coefficient.

The boundary conditions for this simulation were selected to mimic a representative methane gas leak. The gas leak rate was 1 kg/hr injected at a leak height of 1 meter from the ground. A standard log wind profile for the atmospheric boundary layer was used to set the velocity of incoming air:

$$U = \frac{U^*}{\kappa}\ln\left(\frac{z + z_0}{z_0}\right) \tag{2.15}$$

$$U^* = \kappa\frac{U_{ref}}{\ln(\frac{Z_{ref+z_0}}{z_0})}$$

Here, U is the local horizontal wind velocity, κ is the von Karman's constant (0.4), U_{ref} is the known wind velocity at a reference height z_{ref}, and z_0 is the roughness height of the ground (1 meter to simulate tall grasses and vegetation). The reference height was 10 meters. The incoming wind was assumed to have pure air, and the methane leak was assumed pure methane.

2.4.3 Simulation Geometry and Mesh Design

The simulation geometry was selected to be a simple rectangle 1 km wide, 2 km long, and 0.6 km tall. The geometry was designed to simulate half of the plume formation, to take advantage of symmetry laws to reduce computational requirements. Because of the highly multi-scale nature of the simulation, mesh elements were varied from a centimeter to tens of meters to balance simulation fidelity and speediness.

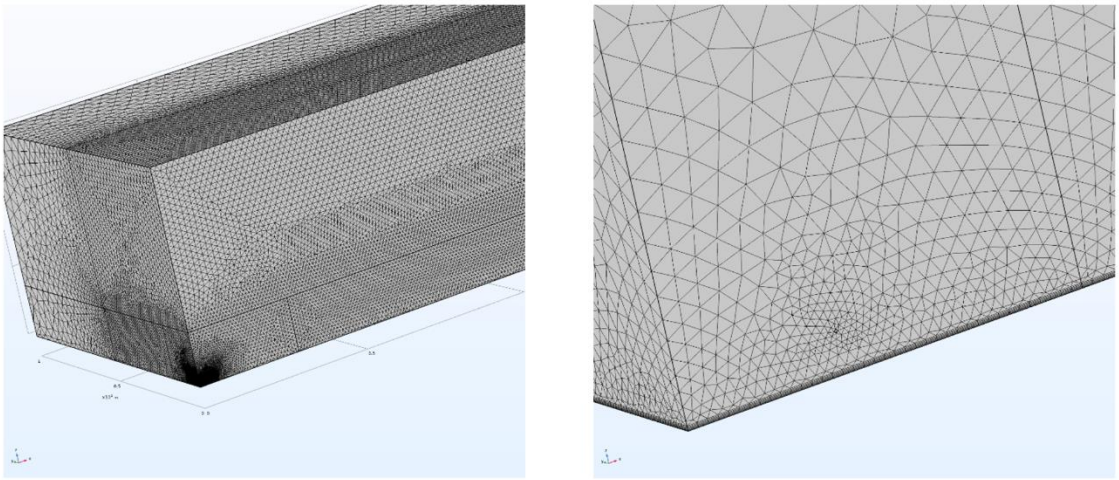

Figure 14. Left: A view of the multi-scale meshing required for this simulation. Note the high density of elements at the initial release of methane, where the methane flow is most dynamic. (Scale in km) Right: 10-meter wide closeup of methane leak source (10 cm diameter) and boundary layer meshing.

The main outcome of these simulation results is a set of plots showing methane concentration along the plume for windspeeds ranging from 2-10 m/s. Figure 15 shows example output, with units of $\log_{10}$ of the mass fraction of methane. In this example, the wind velocity was 10 m/s at a 10 meter reference height (2.8 m/s at the 1-meter release height). Note several streaks of very low mass fraction along the top of the plume. These are likely due to CFD artifacts; they become thinner with more refined meshes.

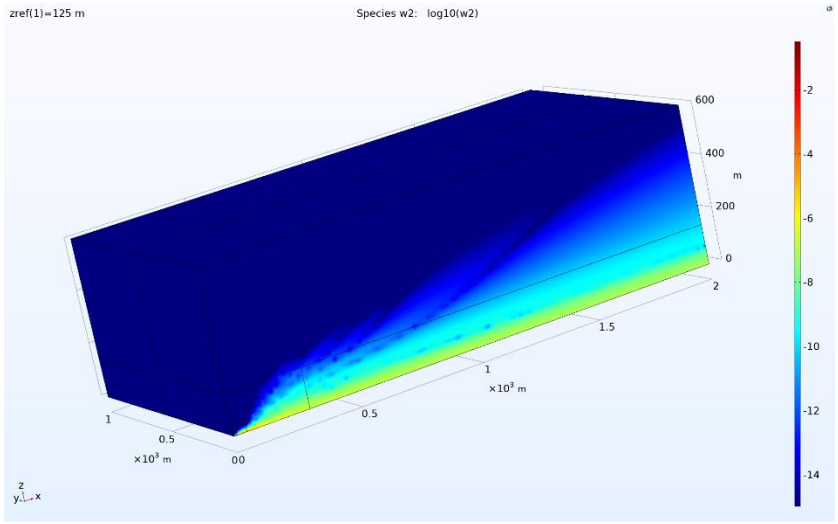

Figure 15. Sample output of methane plume mass fraction plot.

A mesh refinement study was conducted to ascertain the fidelity of the mesh selection with realistic physics. Different meshes were incorporated in the simulation, from ~500,000 elements to more than 5 million elements, and the simulation outputs were compared. Ideally, the simulation results would converge beyond a threshold number of elements. Figure 16 plots mass fraction along the centerline of the plume for different meshes. The mass fractions from all the mesh sizes agree within the first 100 meters in the downwind direction. As this distance is beyond the region where the concentration would be measurable, the mesh sizes used in these studies are sufficient for accurate simulation. At significantly higher release rates, where the detectable concentration would extend further downwind, higher mesh densities would likely be needed. Given the run times of these simulations, more computing resources are likely needed to conduct higher mesh density simulations, such as the use of superclusters and parallel computing.

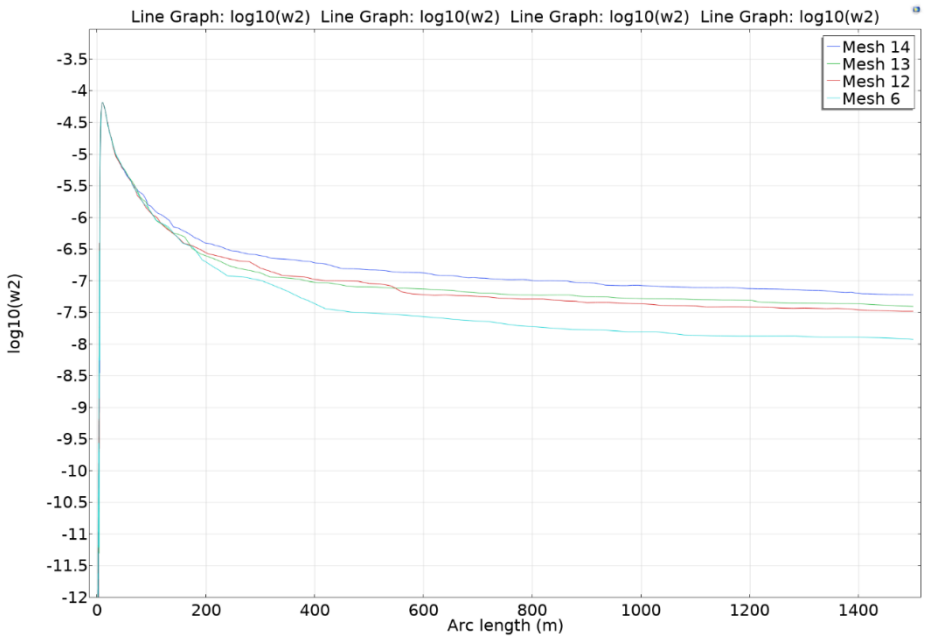

Figure 16. Mass fraction of methane along plume centerline, for different simulation meshes.

2.4.4 Effect of Gravity in the Simulation

Perhaps contrary to normal intuition given the low density of methane, gravity does not play a strong role in the dynamics of the plume, owing to the relatively low concentration of methane for most of the plume (ppm or ppb range). Hence, the bulk fluid flow has relatively uniform densities. The fluid flow appears dominated by the effect of wind. However, two simulations were run to assess the effect of gravity. Figure 17 shows the effect of gravity on the simulation results, where the molecular weight of the gas was varied. The simulations yield identical concentration distributions out to at least 1 km downwind, which is well beyond where the concentration will have become undetectable. The small changes in the concentration distribution beyond 1 km could result from buoyancy differences or computational artifacts of the boundary pressure conditions. The identical behavior of the two simulations within 1 km of the release appears to confirm the hypothesis of gravity's weak effect on plume formation. If gravity were playing a strong role in plume dynamics, it would likely appear closer to the beginning of the plume, where the methane concentration and density gradients are highest.

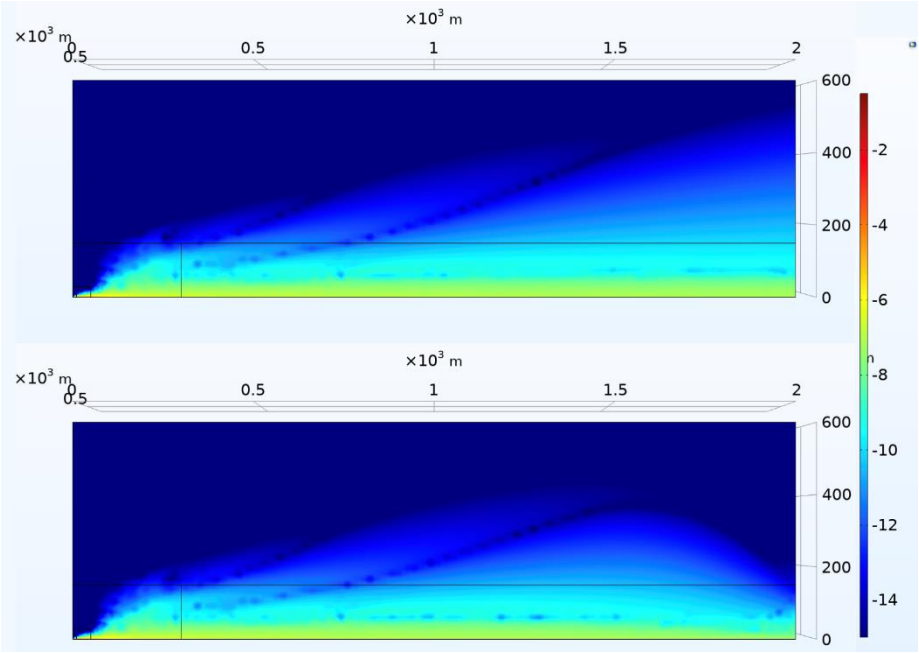

Figure 17. Effect of gravity on of plume dynamics.

2.4.5 Effect of Wind Speed

The concentration distribution of the plume should depend on the local wind speed, which is why leak detection performance is frequently reported as kg/hr *per m/s wind speed*. To confirm that the simulation was correctly capturing this physics, multiple simulations were run with identical parameters other than the wind speed, which was varied from 2.5 m/s to 10 m/s at the 10-meter reference height (0.75 to 2.75 m/s at the 1-meter release height), and the concentration length product across a GSD of a given size at the release point was averaged. Figure 18 shows that the average CL product followed a 1/wind speed behavior exactly, for all GSD sizes studied. This confirms that, for the range of GSDs considered, the simulation results can be used to relate release rate per m/s of wind to a predicted concentration length product.

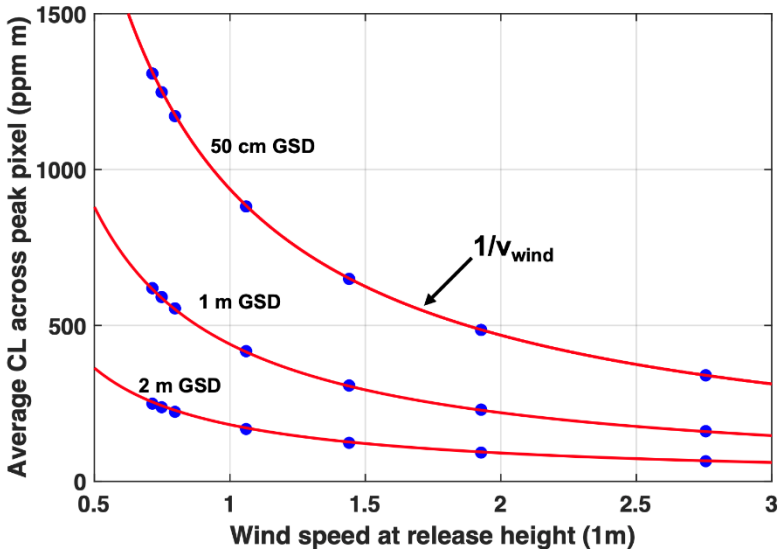

Figure 18. Peak concentration length product vs. wind speed.

2.4.6 Plume Modeling Results

Results of a representative simulation are shown in Figure 19. The top panel shows a vertical slice through the plume along the downwind direction. Peak concentrations at the release point are above 1,000 ppm, but drop to 100 ppm or less about 10 m downwind, as the plume spreads in height and width. The lower panel shows the results of integrating the same simulation along the vertical direction, as a down-looking sensor would do. The concentration length product is about 1,000 ppm-m at the release but drops to the 100s of ppm-m just a few meters downwind. Note that this simulation was performed for 1 kg/hr release rate and a 1 m/s windspeed at the release height. Linear scaling of the concentration can be assumed over the range of relevant release rates. And as shown in Section 2.4.6, doubling the windspeed would halve the integrated CLs.

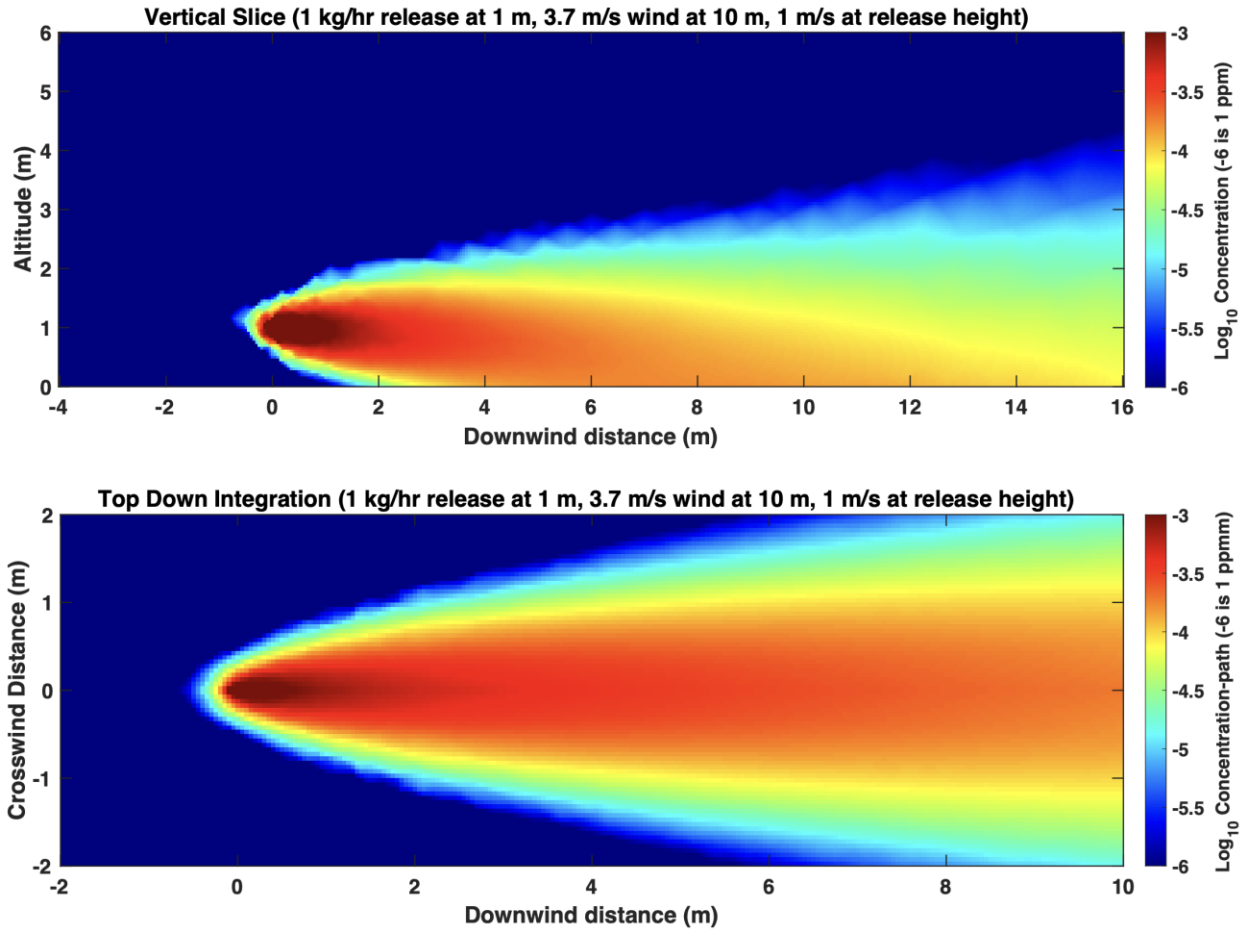

Figure 19. Vertical slice of plume concentration and result of top-down integration.

Finally, Figure 20 shows the results of averaging the concentration-length product near the point of release across varying sized GSDs. The three curves are from three slightly shifted pixel positions, but vary by less than a factor of two and converge as the GSD increases past 5 meters. This plot can be read by considering a particular GSD for a sensor design point. For a one-meter GSD, for example, the 1 kg/hr release rate in a 1 m/s wind results in a peak concentration length product of around 400 ppm-m. Therefore, the point design from Section 2.3 (see Figure 12) with an MDQ of 500 ppm-m°C/Hz$^{1/2}$ would exhibit a minimum detectable leak rate of 1.25 kg/hr per m/s wind in one second for a 1°C ground-plume temperature difference.

A 1/GSD line is provided for comparison, and it is interesting to note that the CL product seems to decrease slightly faster than 1/GSD. This dependence has a system implication: for a fixed number of pixels (fixed data rate), a rectangular focal plane (wider than its height) with narrower IFOV but covering

the same swath will have a higher sensitivity for the same area coverage rate. The smaller pixels increase the sensitivity faster than the reduction in the averaging time (square-root gain) from the reduced number of (along track) pixels that will see the plume and be averaged.

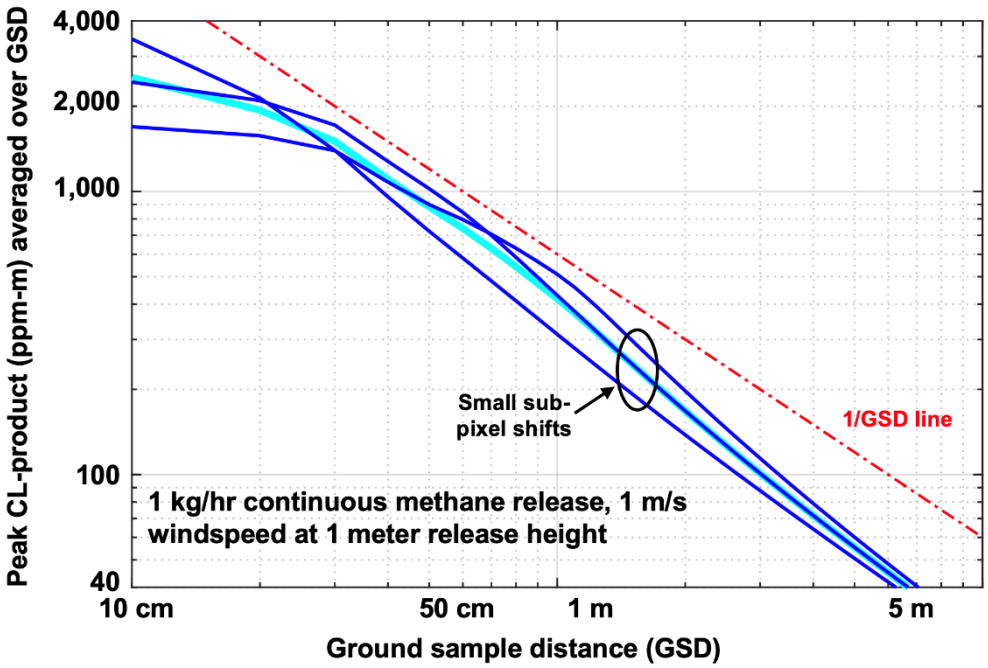

Figure 20. Peak concentration length product vs. GSD.

2.5 OBJECTIVE SYSTEM CONCEPT AND PREDICTED PERFORMANCE

The sensor sensitivity from Section 2.3 can now be combined with the plume results to obtain the predicted minimum detectable leak rate for a given sensor configuration, applying the relation presented in Figure 13.

$$MDRR = \frac{MDQ}{\Delta T} \times \sqrt{\frac{v_p}{N_{pix}^{\parallel} GSD}} \times \left(\frac{RR/v_{wind}}{CL_{peak}} \right) \qquad 2.16$$

Three implementations will be considered: a near-term demonstration system that could be built by the Laboratory in a one-year timeframe, flying at or below 5,000' in a Twin Otter or similar aircraft, and two design points for a notional operational system that would fly higher and use larger (non-COTS) focal planes to obtain higher area-coverage rates. Such a sensor might fly on an uncrewed platform such as an RQ-9, a platform used widely in the DoD and also by NASA. The sensor system characteristics and performance are summarized in Table 6.

Table 6

Performance of Several Sensor Design Points

	Near-Term	Operational	
Platform	Twin Otter	MQ-9	
Altitude	5,000'	10,000'	15,000'
Ground speed	50 m/s	100 m/s	100 m/s
Optics	1.2" F/2.3	1" F/2.3	1.6" F/2.3
GSD	45 cm	1 m	2 m
FPA	640x512, 20 µm	1024x1024, 20 µm	1024x1024, 40 µm
FOV	9°	19°	26°
ACR	41 km^2/hr	370 km^2/hr*	740 km^2/hr
MDRR (Methane, 1°ΔT) per m/s of wind	200 g/hr (5 kg/hr single pixel)	1 kg/hr*	1 kg/hr
MDRR, HCl, /m/s	10 g/hr (day), 600 g/hr (night)	18 g/hr (day) 1 kg/hr (night)	11 g/hr (day) 500 g/hr (night)
MDRR, CO, 5° ΔT, /m/s	50 g/hr	200 g/hr	130 g/hr

* better than 300 g/hr flying at 5,000' for 184 km^2/hr ACR

For all implementations, we assume a newly available SLS (strained-layer superlattice) focal plane sensitive from 2.5 microns to 11.5 microns (spanning both MWIR and LWIR). This enables simultaneous sensitivity to methane and one or two additional MWIR targets, such as hydrogen chloride (HCl), a known effluent from certain illicit drug manufacture, and carbon monoxide (CO), released from gasoline and diesel generators and automobiles. This FPA material is available COTS from Santa Barbara Infrared/IRCameras in a 640x512 format, assumed for the near-term design point. This near-term design also assumes a 9-degree field of view, very close to the 8-degree FOV already demonstrated. Multiple vendors are producing 1024x1024 versions of this FPA material, however, and this is assumed for the operational design points, with larger pixels for larger light collection in one case. The first operational design point has a sensitivity for methane of just under 1 kg/hr at very competitive area coverage rate of 370 km^2/hr, (and noting that the

300 g/hr EPA requirement for mitigation of continuous leaks could be met by flying at a lower altitude and sacrificing area coverage). To increase area coverage rate significantly, a second design point opens the field of view even more to 26° and assumes a similar 1024x1024 focal plane with larger, 40 µm pixel to increase light collection and maintain the 1 kg/hr sensitivity with a larger GSD, yielding an area coverage rate of 740 km^2/hr. The 40 µm pixels would increase the detector noise, but as this system is generally limited by the thermal emission of the optics, this performance can be realized. The 26° field of view with slightly larger pupil would require a particularly large entrance beam splitter, but would otherwise not present significant risk, as we have shown very little field-angle-dependent optical-path error in the interferometer and feel that it can be minimized with appropriate requirements on the beam splitter wedge and relative clocking.

Minimum detectable release rates for hydrogen chloride and carbon monoxide, two gases with absorption bands in the MWIR that are of interest for several DoD/IC missions, are also presented. The sensitivity for hydrogen chloride is exceptionally good as this absorption band is around 3.6 µm, where the majority of the upwelling radiation is from reflected sunlight. At this wavelength region, the self-emission from the plume does not decrease the in-band optical modulation as it does for wavelengths further out in the MWIR and in the LWIR. The lower thermal emission from the ground at 3.6 µm relative to the LWIR makes the nighttime sensitivity for hydrogen chloride worse than for methane, and additional phenomenology study would be required to determine mission relevance.

REFERENCES

[1] National Academies of Sciences, Engineering, and Medicine 2018. Improving Characterization of Anthropogenic Methane Emissions in the United States. Washington, DC: The National Academies Press. https://doi.org/10.17226/24987.

[2] EPA, *Global Non-CO_2 Greenhouse Gas Emission Projections & Mitigation 2015-2020,* EPA-430-R-19-010 (October 2019) https://www.epa.gov/global-mitigation-non-co2-greenhouse-gases

[3] United Nations Environment Programme and Climate and Clean Air Coalition, *Global Methane Assessment: Benefits and Costs of Mitigating Methane Emissions (2021).*

[4] R. B. Lockwood, and M.L. Pieper, "Optimized Optical Performance for an Imaging Spectrometer Applied to Methane Quantification," Annotated charts (1 January 2023).

[5] Saunois, M., Stavert, A. R., Poulter, B., Bousquet, P., Canadell, J. G., Jackson, R. B., Raymond, P. A., Dlugokencky, E. J., Houweling, S., Patra, P. K., Ciais, P., Arora, V. K., Bastviken, D., Bergamaschi, P., Blake, D. R., Brailsford, G., Bruhwiler, L., Carlson, K. M., Carrol, M., Castaldi, S., Chandra, N., Crevoisier, C., Crill, P. M., Covey, K., Curry, C. L., Etiope, G., Frankenberg, C., Gedney, N., Hegglin, M. I., Höglund-Isaksson, L., Hugelius, G., Ishizawa, M., Ito, A., Janssens-Maenhout, G., Jensen, K. M., Joos, F., Kleinen, T., Krummel, P. B., Langenfelds, R. L., Laruelle, G. G., Liu, L., Machida, T., Maksyutov, S., McDonald, K. C., McNorton, J., Miller, P. A., Melton, J. R., Morino, I., Müller, J., Murguia-Flores, F., Naik, V., Niwa, Y., Noce, S., O'Doherty, S., Parker, R. J., Peng, C., Peng, S., Peters, G. P., Prigent, C., Prinn, R., Ramonet, M., Regnier, P., Riley, W. J., Rosentreter, J. A., Segers, A., Simpson, I. J., Shi, H., Smith, S. J., Steele, L. P., Thornton, B. F., Tian, H., Tohjima, Y., Tubiello, F. N., Tsuruta, A., Viovy, N., Voulgarakis, A., Weber, T. S., van Weele, M., van der Werf, G. R., Weiss, R. F., Worthy, D., Wunch, D., Yin, Y., Yoshida, Y., Zhang, W., Zhang, Z., Zhao, Y., Zheng, B., Zhu, Q., Zhu, Q., and Zhuang, Q., "The Global Methane Budget 2000–2017," Earth Syst. Sci. Data, 12, 1561–1623, https://doi.org/10.5194/essd-12-1561-2020, 2020.

[6] APS & OPTICA, Monitoring Methane Emissions from Oil and Gas Operations, Science Policy Report (May 2022) https://www.aps.org/policy/reports/popa-reports/methane.cfm

[7] Duren, R.M., Thorpe, A.K., Foster, K.T., Rafiq, T., Hopkins, F.M., Yadav, V., Bue, B.D., Thompson, D.R., Conley, S., Colombi, N.K., Frankenberg, C., McCubbin, I.B., Eastwood, M.L., Falk, M., Herner, J.D., Croes, B.E., Green, R.O., & Miller, C.E., "California's methane super emitters," Nature, vol. 575 (7 November 2019) https://doi.org/10.1038/s41586-019-1720-3

[8] Lauvaux, T., Giron, C., d'Aspremont, A. Duren, R., Cusworth, D., Shindell, D., Clais, P., "Global assessment of oil and gas methane ultra-emitters," Science vol. 375 (4 February 2022) https://www.science.org/doi/10.1126/science.abj4351

[9] Cusworth, D.H., Duren, R.M., Thorpe, A.K., Olson-Duvall, W., Heckler, J., Chapman, J.W., Eastwood, M.L., Helmlinger, M.C., Green, R.O., Asner, G.P., Dennison P.E., and Miller C.E., "Intermittency of Large Emitters in the Permian Basin," Environmental Science & Technology Letters vol. 8 (2 June 2021) https://pubs.acs.org/action/showCitFormats?doi=10.1021/acs.estlett.1c00173&ref=pdf

[10] Y. Zhang, R. Gautam, S. Pandey, M. Omara, J. D. Maasakkers, P. Sadavarte, D. Lyon, H. Nesser, M. P. Sulprizio, D. J. Varon, R. Zhang, S. Houweling, D. Zavala-Araiza, R. A. Alvarez, A. Lorente, S. P. Hamburg, I. Aben, D. J. Jacob, "Quantifying methane emissions from the largest oil-producing basin in the United States from space," Sci. Adv. 2020, vol. 6 (22 April 2020).

[11] R. A. Alvarez, S. W. Pacala, J. J. Winebrake, W. L. Chameides, and S. P. Hamburg, "Greater focus needed on methane leakage from natural gas infrastructure," PNAS, vol. 109, pp. 6435–6440 (April 24, 2012).

[12] J. B. Ashcom, R.E. Martinez, P.D. Chapnik, R. Standley, C. Monaco, N. Gabardi, C.A. Primmerman, "Airborne Phenomenology (NIFTy): FY2020 Line-Supported Optical Systems Program," Lincoln Project Report LSP-316, (6 May 2021).

[13] J. Ashcom, S. Kaushik, "Wide field of view narrowband imaging filter technology," U.S. Patent 10,794,819 B2, Oct. 6, 2020.

[14] For an introduction to DIAL (Differential Absorption Lidar), see, for example, K.W. Rothe, U. Brinkmann, H. Walther, Applied Physics 3, 115 (1974).

[15] Ashcom, J.B., R.M. Sullenberger P.D. Chapnik, "Narrowband Imaging Filter Technology (NIFTy) Study Final Report" Lincoln Technical Report 1232, (9 July 2018).

[16] Jonathan Franklin, "The MethaneSAT Mission," IWGGMS-17 (14 June 2021).

[17] Johnson, M.R., Tyner, D.R., and Szekeres, A.J., "Blinded evaluation of airborne methane source detection ussing Bridger Photonics LiDAR," Remote Sensing of Environment 259 (2021) https://doi.org/10.1016/j.rse.2021.112418.

[18] Jacob, D.J., Varon, D.J., Cusworth, D.H., Dennison, P.E., Frankenberg, C., Gautam, R., Guanter, L., Kelley, J., McKeever, J., Ott, L.E., Poulter, B., Qu, Z., Thorpe, A.K., Worden, J.R., and Duren, R.M. "Quantifying methane emissions from the global scale down to point sources using satellite

observations of atmospheric methane," Atmospheric Chemistry and Physics Discussions, (11 April 2022) https://doi.org/10.5194/acp-2022-246

[19] http://www.tropomi.eu

[20] https://www.methanesat.org/

[21] https://carbonmapper.org/

[22] Thorpe, A.K., Frenkenberg, C., Aubrey, A.D., Roberts, D.A., Nottrot, A.A., Rahn, T.A., Sauer, J.A., Dubey, M.K., Costigan, K.R., Arata, C., Steffke, A.M., Hills, S., Haselwimmer, C., Charlesworth D., Funk, C.C., Green, R.O., Lundeen, S.R., Boardman, J.W., Eastwood, M.L., Sarture, C.M., Nolte, S.H., McCubbin, I.B., Thompson, D.R., McFadden, J.P., "Mapping methane concentrations from controlled release experiment using the next generation airborne visible/infrared imaging spectrometer (AVRIS-NG)," Remote Sensing of Environment 179 (2016) https://www.sciencedirect.com/science/article/pii/S0034425716301250?via%3Dihub

[23] https://avirisng.jpl.nasa.gov/specifications.html

[24] https://www.bridgerphotonics.com

[25] https://seekops.com/

[26] EPA's Proposal to Reduce Climate- and Health-Harming Pollution from the Oil and Natural Gas Industry (11 November 2021) https://www.epa.gov/controlling-air-pollution-oil-and-natural-gas-industry.

[27] 2000 ASTM Standard Extraterrestrial Spectrum Reference E-490-00 (http://rredc.nrel.gov/solar/spectra/am0/

[28] D. G. Manolakis, R. B. Lockwood, T. W. Cooley, *Hyperspectral Imaging Remote Sensing*, pp. 595-599. Cambridge University Press, Cambridge (2016).

[29] J. B. Ashcom, R.L. Standley, P.D. Chapnik, R.E. Martinez, C. Monaco, N. Gabardi, J.W. Tadiello, C.A. Primmerman, "Airborne Phenomenology (NIFTy): FY2021 Line-Supported Optical Systems Program," Lincoln Project Report LSP-363, (28 June 2022).

REPORT DOCUMENTATION PAGE

Form Approved
OMB No. 0704-0188

1. REPORT DATE *(DD-MM-YYYY)*	**2. REPORT TYPE**	**3. DATES COVERED** *(From - To)*
16-03-2023	Project Report	

4. TITLE AND SUBTITLE

The NIFTy Sensor for Methane Leak Detection Study: FY22 Climate Initiative Technical Investment Program

5a. CONTRACT NUMBER

5b. GRANT NUMBER

5c. PROGRAM ELEMENT NUMBER

6. AUTHOR(S)

J.B. Ashcom, C.A. Primmerman, and G. Ni

5d. PROJECT NUMBER
TI12-0301

5e. TASK NUMBER

5f. WORK UNIT NUMBER

7. PERFORMING ORGANIZATION NAME(S) AND ADDRESS(ES)

MIT Lincoln Laboratory
244 Wood Street
Lexington, MA 02421-6426

8. PERFORMING ORGANIZATION REPORT NUMBER

TIP-189

9. SPONSORING / MONITORING AGENCY NAME(S) AND ADDRESS(ES)

MIT Lincoln Laboratory
244 Wood Street
Lexington, MA 02421-6426

10. SPONSOR/MONITOR'S ACRONYM(S)
MIT LL

11. SPONSOR/MONITOR'S REPORT NUMBER(S)

12. DISTRIBUTION / AVAILABILITY STATEMENT
DISTRIBUTION STATEMENT A. Approved for public release. Distribution is unlimited.

13. SUPPLEMENTARY NOTES

13. ABSTRACT

Methane is a powerful greenhouse gas, roughly 80 times more potent than carbon dioxide in heat-trapping capacity. It is receiving significant attention because reducing methane emissions offers a near-term way to reduce the overall atmospheric greenhouse gas load: a significant fraction of methane input into the atmosphere is anthropogenic, and the lifetime of methane in the atmosphere is relatively short, about nine years. Therefore, reducing the release of methane can be a high-impact path that countries can pursue to meet their commitments to greenhouse-gas reduction. This fact is leading to new regulations on the oil and gas industry as to what levels of natural gas leaks must be searched for and mitigated. In addition, there is renewed attention to increasing our understanding of the worldwide abundance of methane in the atmosphere and, consequently, to better measuring the various natural and manmade sources and sinks. The Climate Initiative-funded FY2022 Methane Study was set up to explore how unique Lincoln Laboratory technology could support methane detection, both for global measurements to support better modeling of climate change, and for wide-area leak detection to support mitigation efforts.

15. SUBJECT TERMS

16. SECURITY CLASSIFICATION OF:			**17. LIMITATION OF ABSTRACT**	**18. NUMBER OF PAGES**	**19a. NAME OF RESPONSIBLE PERSON**
a. REPORT	**b. ABSTRACT**	**c. THIS PAGE**	None	46	**19b. TELEPHONE NUMBER** *(include area code)*
UNCLASSIFIED	UNCLASSIFIED	UNCLASSIFIED			